

# Investigating the Use of Layered Double Hydroxide Nanoparticles as Carriers of Metal Oxides for Theranostics of ROS-Related Diseases

Yajun Liu,<sup>†</sup> Yua Wu,<sup>†</sup> Run Zhang,<sup>†</sup> Jacinta Lam,<sup>‡</sup> Jack C. Ng,<sup>§</sup> Zhi Ping Xu,<sup>†</sup> Li Li,<sup>\*,†</sup> and Hang T. Ta<sup>\*,†,‡,§</sup>

<sup>†</sup>Australian Institute for Bioengineering and Nanotechnology, The University of Queensland, Brisbane, Queensland, Australia 4072

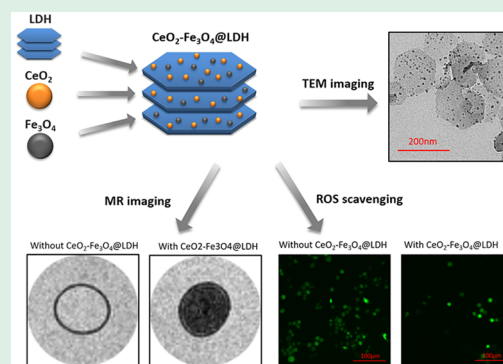
<sup>‡</sup>School of Pharmacy, The University of Queensland, Brisbane, Queensland, Australia 4072

<sup>§</sup>Queensland Alliance for Environment Health Sciences, The University of Queensland, Brisbane, Queensland, Australia 4072

## Supporting Information

**ABSTRACT:** Overproduction of reactive oxygen species (ROS) is commonly known as a key factor in the progression of many chronic inflammation diseases such as atherosclerosis and rheumatoid arthritis. In this study, a metal oxide nanodot-coated layered double hydroxide (LDH) nanocomposite is constructed for theranostics of ROS-related diseases. This is the first time that both cerium oxide and iron oxide nanoparticles (NPs) were attached on the surface of LDH NPs through electrostatic interaction via a nanoengineering approach. LDHs served as nanocarriers, cerium oxide NPs served as therapeutic agents due to the antioxidant properties, and iron oxide NPs served as magnetic resonance imaging (MRI) contrast agents. In vitro studies have demonstrated that the constructed nanocomposites have good biocompatibility, good antioxidant capacity to reduce ROS level in the cells, as well as satisfying cell imaging effect in MRI. Functionalization of LDH surface with cerium oxide NPs and iron oxide NPs allows the simultaneous therapy and diagnosis of ROS-related diseases and may also allow biodistribution tracking of the therapeutic cerium oxide NPs.

**KEYWORDS:** atherosclerosis, macrophage, theranostics, layered double hydroxide, cerium oxide nanoparticle, iron oxide nanoparticle, reactive oxygen species scavenging, magnetic resonance imaging



## INTRODUCTION

Reactive oxygen species (ROS) have been demonstrated to play an important role in human physiological and pathophysiological processes.<sup>1</sup> ROS produced by phagocytic cells such as macrophages and neutrophils generally exert their physiological effects by killing invading pathogens.<sup>2</sup> However, overproduction of ROS can cause dysfunction of tissues and cells and contribute to oxidative stress that accelerates the development of many diseases such as atherosclerosis, diabetes, rheumatoid arthritis, neurodegeneration, and cancer.<sup>3–9</sup> ROS involves in the activation of cell signaling and immune responses. However, the excessive production of ROS can cause oxidative injury and lead to cell death eventually.<sup>10</sup> The ROS family generally includes hydrogen peroxide, hydroxyl radicals, superoxide anions, and hypochlorous acid.<sup>11</sup> They are reported to be linked to various chronic diseases such as cardiovascular diseases.<sup>10</sup> Cellular enzyme oxidants and reductants enable cells to counteract the oxidative injury when excess ROS are produced. However, this cellular defense mechanism can be compromised by diseases or aging.<sup>12</sup> Thus, an effective agent to decrease the cellular ROS levels is urgently needed.

The treatment for ROS-related diseases mainly focuses on therapeutic effect of natural antioxidants based on the

assumption that they will reduce ROS levels in tissues and cells. In fact, the results from the clinical studies using antioxidants such as vitamin E, rottlerin, curcumin, and diclofenac were largely disappointing.<sup>13–17</sup> In recent decades, novel therapeutic drugs like nanomedicine have been designed to inhibit specific ROS-producing systems. Cerium oxide (CeO<sub>2</sub>) NPs have received considerable attention in nanotherapeutics to scavenge mediators like ROS in chronic inflammation due to the excellent antioxidant properties.<sup>18</sup> CeO<sub>2</sub> NPs have shown great superoxide dismutase (SOD) mimetic activity, catalase mimetic activity, hydroxyl radical, and nitric oxide scavenging property.<sup>12</sup> It appears that CeO<sub>2</sub> NPs have the capability of scavenging most types of ROS, making it superior to the antioxidant enzymes that can only specifically inhibit the corresponding catalytic substrate. The excellent antioxidant properties of CeO<sub>2</sub> NPs are attributed to the quick conversion of the oxidation state between Ce<sup>3+</sup> and Ce<sup>4+</sup> on their surfaces.<sup>19</sup>

Molecular imaging techniques are essential to investigate the specific cells and molecules involving in the lesion sites where

**Received:** September 17, 2019

**Accepted:** November 11, 2019

**Published:** November 11, 2019

diseases occur and develop.<sup>20</sup> Magnetic resonance imaging (MRI) has been widely used for disease diagnosis. Several imaging agents including gadolinium and superparamagnetic iron oxide NPs are developed for disease diagnosis. Superparamagnetic iron oxide ( $\text{Fe}_3\text{O}_4$ ) NPs have been widely developed for MRI of diseases.<sup>21–36</sup> Magnetic  $\text{Fe}_3\text{O}_4$  NPs can provide both  $T_1$ -weighted and  $T_2$ -weighted imaging contrast. Unlike gadolinium, magnetic iron oxide NPs exhibiting good biocompatibility, long blood retention, and low cytotoxicity are fit for *in vitro* and *in vivo* diagnostics.<sup>37</sup>

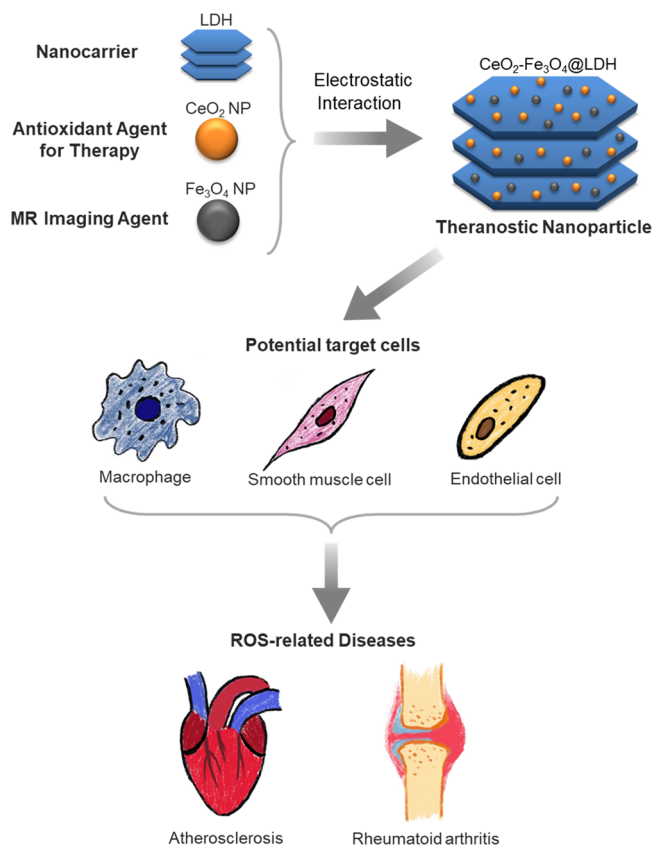
Recently, multifunctional nanocomposites combining drug delivery with imaging probe have provided promising potential due to simultaneously imaging the cells and delivering drugs.<sup>38–41</sup> Layered double hydroxides (LDHs), a type of two dimensional (2D) layered nanomaterials, have been employed as a carrier for drug delivery and bioimaging.<sup>42–45</sup> Moreover, as a unit block, LDHs have been used to construct multifunctional nanocomposites with polymers, NPs, and proteins.<sup>44,46,47</sup> LDHs consist of cationic brucite-like layers and anionic interlayers with the general chemical formula of  $[\text{M}^{\text{II}}_{1-x}\text{M}^{\text{III}}_x(\text{HO})_2]^{x+} [(\text{X}^{n-})_{x/n}\cdot y\text{H}_2\text{O}]^{x-}$ , where  $\text{M}^{\text{II}}$  is the divalent metal cation,  $\text{M}^{\text{III}}$  is the trivalent metal cation, and  $\text{X}^{n-}$  is the intercalating anion.<sup>48</sup> LDHs possess positive charge as  $\text{M}^{\text{II}}$  is partially replaced by  $\text{M}^{\text{III}}$  in the brucite layers. This provides a possibility to conjugate LDHs with negatively charged biomolecules and nanoparticles (NPs). There have been a number of studies on the cooperation between different NPs and LDHs. Li et al. reported  $\text{SiO}_2$  nanodot-coated LDH nanocomposites by attaching  $\text{SiO}_2$  nanodots evenly on LDHs for drug delivery.<sup>49,50</sup> They further modified  $\text{SiO}_2$ -LDH nanocomposites with mannose to achieve targeted siRNA delivery.<sup>44</sup> LDHs were also functionalized with magnetic  $\text{Fe}_3\text{O}_4$  NPs to act as photocatalysts for environmental remediation like water purification because they are capable of adsorption for organic dyes and heavy metal.<sup>51</sup>

In this study, a novel LDH nanocomposite with both cerium oxide NP and magnetic iron oxide NP loading on the surface of LDH was synthesized for biological applications. As shown in Scheme 1, polyacrylic acid (PAA)-stabilized  $\text{CeO}_2$  and  $\text{Fe}_3\text{O}_4$  NPs were first prepared by precipitation approach and then were loaded on the surface of the LDHs to construct  $\text{CeO}_2\text{-Fe}_3\text{O}_4\text{@LDH}$  nanocomposites via electrostatic interaction. LDHs served as nanocarriers that can enhance the half-life of the  $\text{CeO}_2$  and  $\text{Fe}_3\text{O}_4$  NPs in the body,<sup>52</sup>  $\text{CeO}_2$  NPs served as therapeutic agents due to the antioxidant properties, and  $\text{Fe}_3\text{O}_4$  NPs served as contrast agents in MRI to monitor NPs in the cells. Both ROS scavenging and cytotoxicity data showed promising results as well as MRI signal detection in the macrophages. The nanocomposites can be further modified to target ROS-related cells such as macrophages, smooth muscle cells, and endothelial cells. Functionalization of LDH surface with  $\text{CeO}_2$  NPs and  $\text{Fe}_3\text{O}_4$  NPs allows simultaneous therapy and detection of inflammatory diseases such as atherosclerosis and rheumatoid arthritis.

## MATERIALS AND METHODS

**Materials.** Cerium nitrate hexahydrate, PAA ( $M_w = 1800$ ), iron(II) ammonium sulfate, hydrochloric acid (reagent grade, 37%), ammonium hydroxide solution (30%  $\text{NH}_3$  in  $\text{H}_2\text{O}$ ), magnesium chloride, aluminum chloride, hydrogen peroxide, 2,2'-azino-bis(3-ethylbenzothiazoline-6-sulfonic acid) (ABTS), horseradish peroxidase (HRP), and 2',7'-dichlorodihydrofluorescein diacetate (DCF-DA) were purchased from Sigma-Aldrich. Phosphate-buffered saline

## Scheme 1. Schematic Showing the Theranostic Function of $\text{CeO}_2\text{-Fe}_3\text{O}_4\text{@LDH}$ Nanocomposites and Potential Applications in ROS-Related Diseases



(PBS), RPMI 1640 medium, fetal bovine serum (FBS), L-glutamine, penicillin/streptomycin solution, and TrypLE Express were purchased from ThermoFisher Scientific. PrestoBlue cell viability reagent was purchased from Invitrogen.

**Synthesis of Layered Double Hydroxides.** LDHs containing  $\text{Mg}^{2+}$  and  $\text{Al}^{3+}$  ( $[\text{Mg}_2\text{Al}(\text{OH})_6]^+\text{Cl}^-$ ) were prepared by co-precipitation with hydrothermal method.<sup>53</sup> A total of 40 mL of 0.15 M NaOH was added to 10 mL of a mixed solution containing 0.3 M  $\text{MgCl}_2$  and 0.1 M  $\text{AlCl}_3$  and stirred at room temperature for 10 min. The resulting slurry precipitate was collected and washed twice by centrifugation, then dispersed in 40 mL of distilled water. The inhomogeneous suspension was transferred to an autoclave (Teflon-lined stainless steel) and heated at 100 °C for 16 h. The resulting homogeneous suspension was collected and used for subsequent investigations.

**Synthesis of Cerium Oxide NPs.** The PAA-stabilized  $\text{CeO}_2$  NPs were prepared by a precipitation method. A total of 2 mL of a mixed solution containing cerium(III) nitrate (0.4 g) and PAA (0.3 g) was added dropwise to 6 mL of 30% ammonium hydroxide solution with continuous stirring for 24 h. The stirred mixture was then centrifuged at 4000 rpm for 30 min to settle down large agglomerates. The supernatant was collected and purified by dialyzing against 5 L of water at pH 10 for 1 day, followed by dialysis against 5 L of water at pH 7 for another day. The resulting solution was concentrated using a 10K molecular weight cutoff Amicon filter (Millipore, Inc.). The concentration of PAA-coated cerium oxide NPs was measured by inductively coupled plasma mass spectrometry (ICP-MS) analysis (Agilent 7900, Agilent Technologies, Japan).

**Synthesis of Iron Oxide NPs.** The PAA-coated  $\text{Fe}_3\text{O}_4$  NPs were prepared by co-precipitation method. Typically, 0.2 g of PAA was dissolved in 50 mL of Milli-Q water. The PAA solution was purged with nitrogen for 30 min and then heated at 130 °C to reflux using an oil bath. A mixture of 0.51 mM  $\text{FeCl}_3\cdot 6\text{H}_2\text{O}$  (0.14 g) and 0.25 mM

$(\text{NH}_4)_2\text{Fe}(\text{SO}_4)_2 \cdot 6\text{H}_2\text{O}$  (0.10 g) was dissolved in 1 mL of 37% concentrated HCl. The mixed solution was then quickly added into the hot PAA solution. After stirring for 5 min, 15 mL of 30% concentrated ammonia solution was added into the mixture, followed by refluxing the solution for 2 h. The resulting solution was concentrated using a 50K molecular weight cutoff Amicon filter (Millipore, Inc.). The concentrated solution was then dialyzed against 5 L of water at pH 10 for 1 day and pH 7 for 3 days. The PAA-coated  $\text{Fe}_3\text{O}_4$  NPs were collected and stored at 4 °C. The concentration of PAA-coated  $\text{Fe}_3\text{O}_4$  NPs was measured using ICP-MS.

**Synthesis of  $\text{CeO}_2\text{-Fe}_3\text{O}_4\text{@LDH}$  Nanocomposites.** The prepared LDHs,  $\text{CeO}_2$ , and  $\text{Fe}_3\text{O}_4$  NP suspensions were adjusted to the concentration of 1 mg/mL. A certain volume of LDH suspension was dropwise added into a mixture of  $\text{CeO}_2$  and  $\text{Fe}_3\text{O}_4$  suspension under continuous stirring for 24 h. The resulting solution was centrifuged at 14,000 rpm for 15 min and washed with water twice. Finally, the pellets were resuspended in 2 mL of Milli-Q water.

**Dynamic Light Scattering.** The hydrodynamic particle size, size distribution, and  $\zeta$  potential of LDHs,  $\text{CeO}_2$  NPs,  $\text{Fe}_3\text{O}_4$  NPs, and  $\text{CeO}_2\text{-Fe}_3\text{O}_4\text{@LDH}$  nanocomposites were determined by dynamic light scattering (DLS) using DTS1070 folded capillary cell (Malvern) on a Malvern Zetasizer. Each sample was measured at 25 °C in triplicate using the parameter settings as follows with water as dispersant and a measurement angle of 173° backscatter. For LDHs and LDH nanocomposites, refractive index = 1.550, absorption = 0.000; for cerium oxide NPs, refractive index = 2.2, absorption = 0.001; for iron oxide NPs, refractive index = 2.42, absorption = 0.001.

**Transmission Electron Microscopy.** Transmission electron microscopy (TEM) images were captured on an HT7700 Transmission Electron Microscope (Hitachi) at an accelerating voltage of 100 kV. TEM sample was prepared in 100% ethanol and dried on the carbon film-coated copper grid (Zhongjingkeyi Technology Co., Japan).

**Energy-Dispersive X-ray Spectroscopy.** Energy-dispersive X-ray spectroscopy (EDS) images were obtained on an HT7700 transmission electron microscope (Hitachi) and analyzed on an XFlash6TI60 (Bruker). EDS sample was prepared in 100% ethanol and dried on the carbon film-coated copper grid (Zhongjingkeyi Technology Co., Japan).

**Inductively Coupled Plasma Mass Spectrometry.** The elemental concentrations in each sample were determined using inductively coupled plasma-mass spectrometry using a ICP-MS apparatus (Agilent 7900, Agilent Technologies, Japan). Mg and Al levels in LDH-contained solution were used for determining the concentration of LDH. Based on the chemical formula of LDH ( $[\text{Mg}_2\text{Al}(\text{OH})_6]^{+}\text{Cl}^{-}$ ),<sup>53</sup> the molecular weight of LDH is identified to be 213.092 g/mol. The concentration of  $\text{CeO}_2$  NPs and  $\text{Fe}_3\text{O}_4$  NPs was determined by Ce and Fe, respectively. The estimation of  $\text{CeO}_2$  or  $\text{Fe}_3\text{O}_4$  NP percentage loading on the LDH was calculated using the following equation:

$$\text{NP loading efficiency (\%)} = \frac{\text{concentration of NPs obtained by ICP} - \text{MS}}{\text{theoretical concentration of NP for synthesis}} \times 100\%$$

where theoretical concentration of NPs is the concentration of the NPs used in the synthesis.

**Fourier-Transform Infrared Spectroscopy.** Fourier-transform infrared spectroscopy (FTIR) spectra were analyzed on a Nicolet 5700 FT-IR apparatus. Samples were prepared in the form of powder.

**Anti-ROS Capability of  $\text{CeO}_2\text{-Fe}_3\text{O}_4\text{@LDH}$  Nanocomposites.**  $\text{CeO}_2\text{-Fe}_3\text{O}_4\text{@LDH}$  nanocomposites with different concentrations of  $\text{CeO}_2$  (0.5, 1, 5, 20, and 40  $\mu\text{g}/\text{mL}$ ) were treated with 0.1 mM  $\text{H}_2\text{O}_2$  in a 96-well plate and incubated for 1 h at 37 °C with 200 rpm shaking in a total volume of 25  $\mu\text{L}$ . 25  $\mu\text{L}$  of HRP (0.01 U) was added into each reaction, followed by 10 min incubation at room temperature. 50  $\mu\text{L}$  of ABTS (10 mg/mL) was then added into the reaction, and the absorbance of samples at 405 nm was immediately measured by microplate reader Tecan X200. The absorbance of 0  $\mu\text{g}/\text{mL}$  sample was determined as 0% ROS scavenging.

**Cell Culture.** Macrophage J774A.1 and Chinese hamster ovary (CHO) cell lines were attained from American Type Culture Collection (ATCC). Macrophages were cultured in RPMI1640 medium supplemented with 10% FBS, 1% L-glutamine and penicillin (10 U/mL)/streptomycin (10  $\mu\text{g}/\text{mL}$ ) in an incubator at 37 °C with 5%  $\text{CO}_2$ . CHO cells were cultured in DMEM medium with 10% FBS and penicillin (10 U/mL)/streptomycin (10  $\mu\text{g}/\text{mL}$ ). Cell numbers were counted using a Beckman Coulter Z Series instrument.

**In Vitro ROS Scavenging Assay.** Cellular ROS was evaluated with 2',7'-dichlorofluorescein diacetate (DCFDA). When diffusing into the cell, DCFDA is deacetylated to a nonfluorescent compound and subsequently oxidized by ROS into the fluorescent 2',7'-dichlorofluorescein (DCF).<sup>54</sup> Thus the fluorescent signal intensity can directly reflect and positively correlate with intracellular ROS level. To trigger the ROS production from macrophages,  $\text{H}_2\text{O}_2$  as a stimulus can pass through the macrophage membranes and stimulate the generation of hydroxyl radicals ( $\text{OH}\bullet$ ), which induces oxidative stress and cellular damage.<sup>55</sup> Our aim is to detect the fluorescence intensity and determine whether the intracellular ROS can be quenched by the desired NPs. Macrophages were seeded in 96-well tissue-treated plates at a density of 10,000 cells per well. After 24 h incubation, macrophages were treated with  $\text{CeO}_2$  NPs at the concentration ranging from 0.5 to 1  $\mu\text{g}/\text{mL}$ . The concentration of  $\text{CeO}_2\text{-Fe}_3\text{O}_4\text{@LDH}$  was determined based on the content of  $\text{CeO}_2$  attached on the surface of LDH. After 4 h of treatment with NPs to allow NP uptake by macrophages, the NP solution was removed, followed by adding 100  $\mu\text{L}$  of DCFDA (25  $\mu\text{M}$  final concentration) diluted in PBS. Macrophages were then stained with DCFDA for 45 min and washed with PBS once. The intracellular levels of ROS were stimulated by 0.05 mM or 0.5 mM  $\text{H}_2\text{O}_2$  dissolved in PBS and determined by recording the fluorescence intensity at time points of 15 min after adding  $\text{H}_2\text{O}_2$ . Fluorescence intensity was measured (excitation/emission = 485/535 nm) using an EnSpire Alpha multimode plate reader (PerkinElmer). The background fluorescence value containing cell-only control wells was subtracted from the fluorescence value of each experimental well. ROS levels were calculated using the following equation:

$$\text{ROS level (fold change)} = \frac{F_{\text{stimulation}}}{F_{\text{control}}}$$

where  $F_{\text{stimulation}}$  is the fluorescence intensity of the cells stimulated by  $\text{H}_2\text{O}_2$  and  $F_{\text{control}}$  is the fluorescence intensity of the cells treated with DCFDA only without any additional stimulation. The fluorescence images were taken by Nikon ECLIPSE Ti microscopy system with Photometrics Coolsnap HQ2 camera and Nikon INTENSILIGHT C-HGFI fluorescent light source.

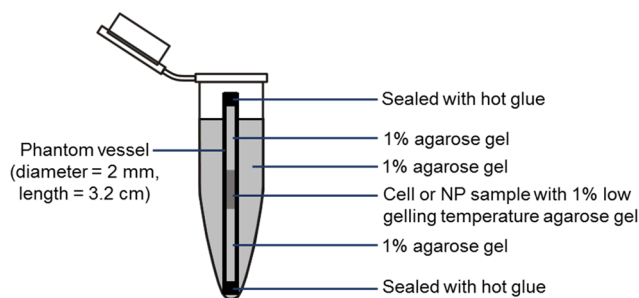
**In Vitro Cytotoxicity Assay.** Cell viability was determined using PrestoBlue cell viability reagent (Invitrogen). Macrophages were seeded in 96-well tissue-treated plates at a density of 10,000 cells per well. After 24 h incubation, the cells were treated with  $\text{CeO}_2\text{-Fe}_3\text{O}_4\text{@LDH}$  at the concentration of  $\text{CeO}_2$  ranging from 0.1 to 1  $\mu\text{g}/\text{mL}$ . The concentration of  $\text{Fe}_3\text{O}_4$  NPs, LDHs, or  $\text{CeO}_2\text{-Fe}_3\text{O}_4\text{@LDH}$  was determined based on the content of  $\text{CeO}_2$  attached on the surface of LDH. After 24 h treatment with NPs, the NP solution was removed, followed by adding 10  $\mu\text{L}$  of PrestoBlue into the total volume of 100  $\mu\text{L}$  of culture medium to each well. The cells were then incubated at 37 °C for 30 min. Fluorescence intensity was measured at the excitation wavelength of 535 nm (25 nm bandwidth) and the emission wavelength of 615 nm (10 nm bandwidth) after incubation using an EnSpire Alpha multimode plate reader (PerkinElmer, USA). The background fluorescence value containing no-cell control wells was subtracted from the fluorescence value of each experimental well. Cell viability was calculated using the following equation:

$$\text{cell viability (\%)} = \frac{F_{\text{sample}}}{F_{\text{control}}} \times 100\%$$

where  $F_{\text{sample}}$  was the fluorescence intensity of the cells treated with different conditions and  $F_{\text{control}}$  was the fluorescence intensity of the cells cultured in the standard medium without any treatment.

**Magnetic Resonance Imaging.** Macrophages were seeded in 6-well tissue-treated plates at a density of  $3 \times 10^5$  cells per well. After 24 h incubation, the cells were treated with  $\text{CeO}_2\text{-Fe}_3\text{O}_4\text{@LDHs}$  at the concentration of 0, 0.5, and 1  $\mu\text{g/mL}$  based on the amount of  $\text{CeO}_2$  conjugated to the LDH. After an additional 8 h incubation, the NP solution was removed followed by washing cells with PBS once. The cells were then detached by TrypLE Express and centrifuged at 200 g for 5 min. TrypLE Express was removed after washing cells with PBS at 200 g for 5 min. The cells were subsequently resuspended with 20  $\mu\text{L}$  of warm 1% low-gelling temperature agarose and quickly transferred into the prepared phantom vessel. To prepare the phantom vessel, the lower end of a straw with 3.2 cm long was sealed with hot glue, followed by adding around 100  $\mu\text{L}$  of warm 1% agarose gel into the phantom vessel (see Scheme 2). After gel

### Scheme 2. Schematic Illustration of the Preparation of Phantom Vessel for MRI



solidification for 10 min, the cell sample or NP sample was quickly added onto the agarose gel as mentioned before. Any bubble formed in the tubes was popped by a small needle, as it could influence the MRI signal. The cell pellet was set for 10 min, and then warm 1% agarose gel was added on the top of the cell pellet gelling for 10 min. Subsequently, the top end of the phantom vessel was sealed with hot glue. The prepared phantom vessel was embedded in a 1.5 mL Eppendorf tube containing 1% agarose gel. MRI was performed on a 9.4 T MRI scanner (Bruker).  $T_2$ -weighted images were captured under the following parameter settings: TR = 2630.0 ms, TE = 53.1 or 100 ms, FA =  $90.0^\circ$ , and TA = 0 h 11 m 13 s 261 ms NEX 1.

**Statistical Analysis.** Data are presented as mean  $\pm$  SD from at least three independent experiments and analyzed with two-way ANOVA or one-way ANOVA. The level of statistical significance was defined as  $p$ -value  $< 0.05$ . The graphs were plotted using GraphPad Prism 7 software (GraphPad Prism Inc. CA, USA).

## RESULTS AND DISCUSSION

**Physicochemical Features of  $\text{CeO}_2$ ,  $\text{Fe}_3\text{O}_4$ , LDH, and  $\text{CeO}_2\text{-Fe}_3\text{O}_4\text{@LDH}$  Nanocomposites.** Monodispersed PAA-stabilized  $\text{CeO}_2$  and PAA-stabilized  $\text{Fe}_3\text{O}_4$  NPs were prepared via precipitation method. DLS data in Table 1 and Figure 1a,b indicated that  $\text{CeO}_2$  and  $\text{Fe}_3\text{O}_4$  NPs had narrow size distribution with the particle sizes in the range of 10–11 and 12–13 nm and  $\zeta$  potentials of  $-21.0$  and  $-17.0$  mV, respectively. The TEM images in Figure 1e showed  $\text{CeO}_2$

**Table 1. Characteristics of  $\text{CeO}_2$ ,  $\text{Fe}_3\text{O}_4$ , LDHs, and  $\text{CeO}_2\text{-Fe}_3\text{O}_4\text{@LDH}$  Nanocomposites Measured by DLS Zetasizer**

sample	polydispersity index	Z-average (d, nm)	$\zeta$ potential (mV)
$\text{CeO}_2$	$0.379 \pm 0.071$	$11.1 \pm 0.8$	$-23.2 \pm 2.1$
$\text{Fe}_3\text{O}_4$	$0.339 \pm 0.013$	$12.0 \pm 0.9$	$-15.2 \pm 2.4$
LDH	$0.132 \pm 0.016$	$113.1 \pm 1.1$	$40.1 \pm 0.3$
$\text{CeO}_2\text{:Fe}_3\text{O}_4\text{:LDH}$ 1:4:4	$0.140 \pm 0.017$	$170.9 \pm 0.4$	$-18.7 \pm 0.1$

and  $\text{Fe}_3\text{O}_4$  NPs exhibited irregular shapes. As shown in Figure S1a, the powder X-ray diffraction (XRD) patterns of the synthesized  $\text{CeO}_2$  NPs exhibited very broad peaks at 28.4, 47.5, and 56.3, corresponding to (111), (220), and (311) planes of  $\text{CeO}_2$  with a cubic fluorite structure.<sup>56</sup> The broad diffraction peaks of  $\text{CeO}_2$  NPs are ascribed to the small particle size of  $\text{CeO}_2$  and PAA polymer coating. The XRD patterns of  $\text{Fe}_3\text{O}_4$  NPs showed  $\text{Fe}_3\text{O}_4$  NPs have inverse cubic spinel phase as displaying a series of characteristic peaks (220), (311), (400), (422), (511), and (440).<sup>57</sup> Well-dispersed LDHs, possessing hexagonal shapes (Figure 1e), were obtained with the particle sizes of approximately 113 nm and the  $\zeta$  potential of  $+42.5$  mV (Table 1 and Figure 1a,b), as reported previously.<sup>58</sup> As shown in Figure S1b, LDHs showed strong XRD peaks, indexing as typical (003) and (006) peaks of LDHs. LDHs exhibited the typical layered features with a rhombohedral symmetry in accordance with our previous report.<sup>53</sup>

To obtain the desired  $\text{CeO}_2\text{-Fe}_3\text{O}_4\text{@LDH}$  nanocomposites, the mass ratios of  $\text{CeO}_2$  to LDH and  $\text{Fe}_3\text{O}_4$  to LDH were first investigated.  $\text{CeO}_2\text{@LDHs}$  synthesized under the mass ratios of 4:1, 2:1, 1:1, and 1:2 shared the similar particle sizes and  $\zeta$  potentials, while the particles become much bigger at the mass ratio of 1:4 due to the particle aggregation (see Figure S2a,b). As for  $\text{Fe}_3\text{O}_4\text{@LDHs}$ , the particle sizes of the three tested particles at the mass ratios of 8:1, 4:1, and 2:1 were similar (see Figure S2c,d), while the particles were aggregated macroscopically at the mass ratio of 1:1, which was not being tested via DLS technique. Then the optimized mass ratios of  $\text{CeO}_2\text{@LDHs}$  and  $\text{Fe}_3\text{O}_4\text{@LDHs}$  were determined to 1:2 and 2:1, respectively. The TEM images in Figure S2e,f showed the successful loading of  $\text{CeO}_2$  on the LDH with the mass ratio of 1:2 and  $\text{Fe}_3\text{O}_4$  on the LDH with the mass ratio of 2:1 (or 4:2). Thus, we combined these two for the synthesis of  $\text{CeO}_2\text{-Fe}_3\text{O}_4\text{@LDH}$  nanocomposites, and the theoretical desired mass ratio of  $\text{CeO}_2$  to  $\text{Fe}_3\text{O}_4$  to LDH could be presumed as 1:4:4. Then, we properly mixed LDH NP suspension with the  $\text{CeO}_2$  and  $\text{Fe}_3\text{O}_4$  mixture dropwise at the mass ratio of 1:4:4 for  $\text{CeO}_2$  to  $\text{Fe}_3\text{O}_4$  to LDH. As shown in Figure 1c, the hydrodynamic size of  $\text{CeO}_2\text{-Fe}_3\text{O}_4\text{@LDH}$  increased to 170 nm due to the slight aggregation, and  $\zeta$  potential was reversed to  $-18.7$  mV. TEM images displayed that  $\text{CeO}_2$  and  $\text{Fe}_3\text{O}_4$  nanodots were evenly distributed on the surface of LDHs and  $\text{CeO}_2\text{-Fe}_3\text{O}_4\text{@LDH}$  nanocomposites retained the hexagonal and layered shapes. XRD results in Figure S1b also showed  $\text{CeO}_2\text{-Fe}_3\text{O}_4\text{@LDH}$  nanocomposites have similar diffraction peaks as LDHs in accordance with TEM results that  $\text{CeO}_2\text{-Fe}_3\text{O}_4\text{@LDH}$  nanocomposites retained a layered structure. Ce and Fe spectrum were also observed via energy-dispersive X-ray spectrometry (EDS) coupled with TEM (see Figure S3), indicating the existence of both  $\text{CeO}_2$  and  $\text{Fe}_3\text{O}_4$  NPs on LDHs. The even attachment of  $\text{CeO}_2\text{-Fe}_3\text{O}_4$  on LDHs is attributed to the electrostatic interaction and space confinement.<sup>59</sup>

Different mass ratios of  $\text{CeO}_2$  to  $\text{Fe}_3\text{O}_4$  to LDH (1:4:2, 1:8:4, and 1:8:2) were also investigated to further confirm whether the optimized ratio would be 1:4:4. As shown in Figure S4 and Table S1,  $\text{CeO}_2\text{-Fe}_3\text{O}_4\text{@LDH}$  nanocomposites at different mass ratios of  $\text{CeO}_2$  to  $\text{Fe}_3\text{O}_4$  to LDH displayed similar size distributions and  $\zeta$  potentials. The TEM images in Figure S4 revealed that  $\text{CeO}_2$  and  $\text{Fe}_3\text{O}_4$  NPs were attached on LDHs. The loading amount of both  $\text{CeO}_2$  NPs and  $\text{Fe}_3\text{O}_4$  NPs was further tested using ICP-MS. Among the four NPs,  $\text{CeO}_2$

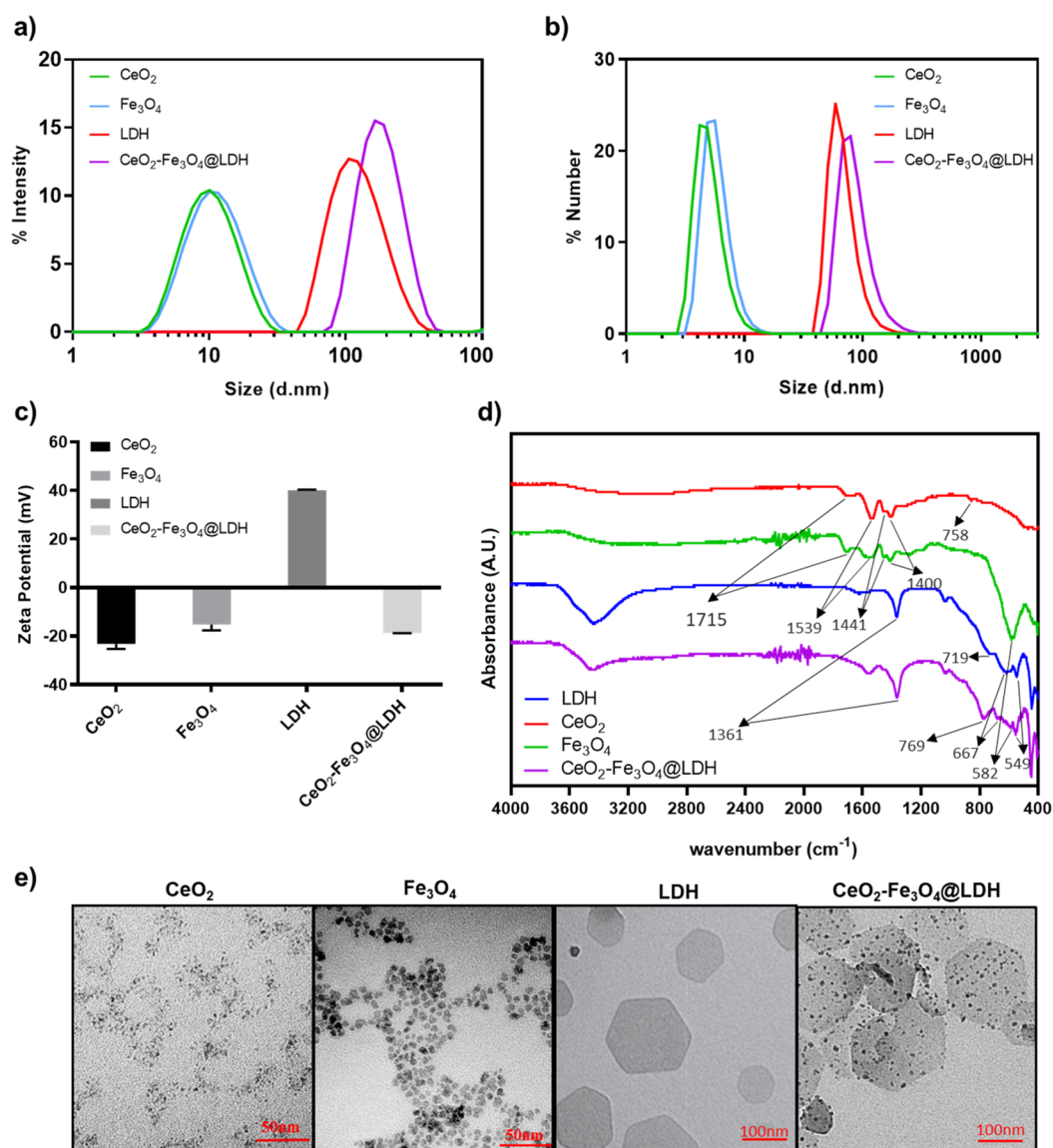


**Figure 1.** Characteristics of CeO<sub>2</sub>, Fe<sub>3</sub>O<sub>4</sub>, LDHs, and CeO<sub>2</sub>-Fe<sub>3</sub>O<sub>4</sub>@LDH nanocomposites. (a–c) The size distribution by intensity, number and  $\zeta$  potential of CeO<sub>2</sub>, Fe<sub>3</sub>O<sub>4</sub>, LDHs, and CeO<sub>2</sub>-Fe<sub>3</sub>O<sub>4</sub>@LDH nanocomposites by DLS. (d) FTIR spectra (4000–400 cm<sup>-1</sup> region) of CeO<sub>2</sub>, Fe<sub>3</sub>O<sub>4</sub>, LDHs, and CeO<sub>2</sub>-Fe<sub>3</sub>O<sub>4</sub>@LDH nanocomposites. (e) The TEM images of CeO<sub>2</sub>, Fe<sub>3</sub>O<sub>4</sub>, LDHs, and CeO<sub>2</sub>-Fe<sub>3</sub>O<sub>4</sub>@LDH nanocomposites.

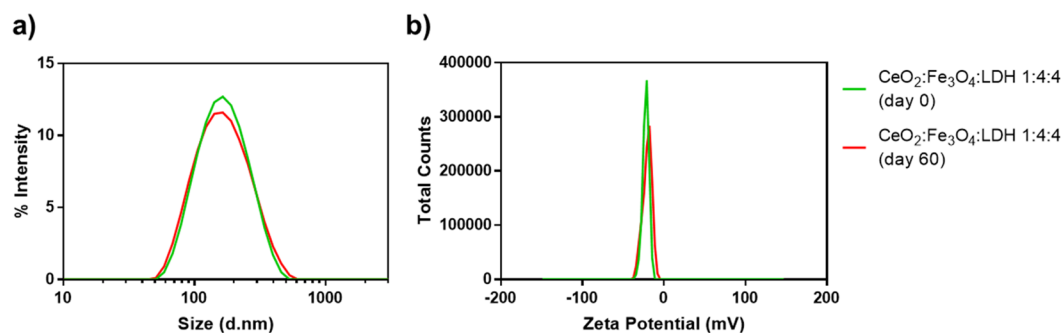


**Figure 2.** Size distribution (a) and  $\zeta$  potential (b) of CeO<sub>2</sub>-Fe<sub>3</sub>O<sub>4</sub>@LDH nanocomposites synthesized at day 0 and day 60.

Fe<sub>3</sub>O<sub>4</sub>@LDH nanocomposites at the mass ratio of 1:4:4 for CeO<sub>2</sub> to Fe<sub>3</sub>O<sub>4</sub> to LDH exhibited the highest yield of CeO<sub>2</sub> NPs (7.71  $\mu$ g/mL) and Fe<sub>3</sub>O<sub>4</sub>NPs (18.73  $\mu$ g/mL). Thus, the optimized mass ratio of CeO<sub>2</sub> to Fe<sub>3</sub>O<sub>4</sub> to LDH to make CeO<sub>2</sub>-Fe<sub>3</sub>O<sub>4</sub>@LDH nanocomposites would be 1:4:4, used for

further modification, characterization, and other tests unless stated.

FTIR spectrometry has further verified the loading of CeO<sub>2</sub> and Fe<sub>3</sub>O<sub>4</sub> NPs on the LDHs. As shown in Figure 1d, the characteristic bands of CeO<sub>2</sub> and Fe<sub>3</sub>O<sub>4</sub> NPs at 1715, 1539,

1441, and 1440  $\text{cm}^{-1}$  are assigned to C=O stretch, C–H stretch, O–H stretch, and N–O stretch, respectively.<sup>60</sup> These peaks were attributed to PAA polymer, suggesting  $\text{CeO}_2$  and  $\text{Fe}_3\text{O}_4$  NPs are stabilized by PAA coating.<sup>61</sup> The absorption band at 758  $\text{cm}^{-1}$  corresponds to Ce–O stretching vibration.<sup>61</sup> The specific band at 582  $\text{cm}^{-1}$  attributes to Fe–O stretching vibration.<sup>62</sup> The FTIR spectrum of LDH shows three strong peaks at 719, 667, and 549  $\text{cm}^{-1}$  corresponding to O–M–O bending vibrations.<sup>63</sup> An additional peak at 1361  $\text{cm}^{-1}$  is found in LDH due to the carbonate formation.<sup>64</sup> After coating  $\text{CeO}_2$  and  $\text{Fe}_3\text{O}_4$  NPs, the characteristic peaks of  $\text{CeO}_2$  and  $\text{Fe}_3\text{O}_4$  NPs at 758 and 582  $\text{cm}^{-1}$  were also observed in  $\text{CeO}_2\text{-Fe}_3\text{O}_4\text{@LDH}$  nanocomposites, suggesting that  $\text{CeO}_2$  and  $\text{Fe}_3\text{O}_4$  NPs were coated on the surface of LDHs.

The stability of  $\text{CeO}_2\text{-Fe}_3\text{O}_4\text{@LDH}$  nanocomposites were further examined for 60 days. As shown in Figure 2, the size, size distribution and  $\zeta$  potential of  $\text{CeO}_2\text{-Fe}_3\text{O}_4\text{@LDH}$ s remained stable after two months, indicating the favorable stability of the desired NPs.

**ROS Scavenging Capability of  $\text{CeO}_2\text{-Fe}_3\text{O}_4\text{@LDH}$  Nanocomposites.** Our previous studies showed that  $\text{CeO}_2$  loaded hybrid NPs have anti-ROS properties in the ABTS-HRP system.<sup>25</sup> Briefly,  $\text{CeO}_2$  loaded hybrid NPs can scavenge and inhibit ROS such as hydrogen peroxide and superoxide radical in the solution system along with the cerium oxide NPs swift between  $\text{Ce}^{3+}$  and  $\text{Ce}^{4+}$ . Here, we investigated the ROS scavenging capability of  $\text{CeO}_2\text{-Fe}_3\text{O}_4\text{@LDH}$  nanocomposites. As shown in Figure 3,  $\text{CeO}_2\text{-Fe}_3\text{O}_4\text{@LDH}$  nanocomposites could significantly reduce the ROS level with a quenching ability up to 40% when the concentration of Ce reached to 40  $\mu\text{g}/\text{mL}$ .

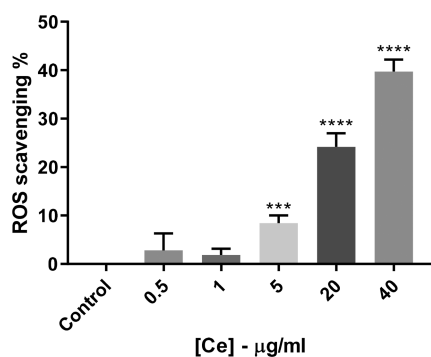


**Figure 3.** ROS scavenging capability of  $\text{CeO}_2\text{-Fe}_3\text{O}_4\text{@LDH}$  nanocomposites. Different concentrations of  $\text{CeO}_2\text{-Fe}_3\text{O}_4\text{@LDH}$ s were tested in the ABTS-HRP system. The absorbance of the different samples was detected by Tecan X200. Control group is the one without nanocomposites determined as 0% of scavenging. Results were analyzed by one-way ANOVA. Data are presented as mean  $\pm$  SD, \*\*\* $p$  < 0.001 versus control, \*\*\*\* $p$  < 0.0001 versus control,  $n = 6$ .

**In Vitro ROS Scavenging by  $\text{CeO}_2\text{-Fe}_3\text{O}_4\text{@LDH}$  Nanocomposites.** Macrophages are used in *in vitro* study as they produce excessive ROS when the immune system responds to the atherosclerotic lesions. Toxic ROS can further accelerate the development of atherosclerosis.<sup>65</sup> Our aim is to decrease the ROS level in the macrophages and then inhibit the downstream regulation induced by toxic ROS. Before determining the ROS scavenging capability of the desired  $\text{CeO}_2\text{-Fe}_3\text{O}_4\text{@LDH}$  nanocomposites in macrophages J774.1, it is imperative to confirm the efficacy of  $\text{CeO}_2$  NPs on quenching the ROS as reported in the previous study.<sup>66</sup> Our study has proved that ROS was significantly scavenged at the  $\text{CeO}_2$  concentrations of 0.5 and 1  $\mu\text{g}/\text{mL}$  after stimulating cells with 0.5 mM  $\text{H}_2\text{O}_2$  for 15–20 min (Figure S5). Notably, very high concentration of  $\text{CeO}_2$  (20  $\mu\text{g}/\text{mL}$ ) did not provide a satisfactory scavenging effect, which might be due to the increasing toxicity to the macrophages. It was reported that at high concentrations, the NPs are toxic to the cells and trigger the elevation of ROS.<sup>67</sup> The data suggest that an appropriate dosing is essential to effectively quench the ROS, thus  $\text{CeO}_2\text{-Fe}_3\text{O}_4\text{@LDH}$ s (1:4:4) containing  $\text{CeO}_2$  NPs at 0.5 and 1  $\mu\text{g}/\text{mL}$  were chosen to evaluate the ROS quenching capability of the combined NPs in the macrophages. The composition of the combined NPs is shown in Table 2. ROS levels were significantly quenched in  $\text{CeO}_2$ -pretreated as well as in  $\text{CeO}_2\text{-Fe}_3\text{O}_4\text{@LDH}$ -pretreated macrophages with 0.5 mM  $\text{H}_2\text{O}_2$  stimulating (see Figure 4a,b), suggesting a promising application for the desired  $\text{CeO}_2\text{-Fe}_3\text{O}_4\text{@LDH}$ s. It was noted that the ROS quenching effect did not increase when the nanocomposite concentration increased from 0.5 to 1  $\mu\text{g}/\text{mL}$  (concentrations based on  $\text{CeO}_2$ ).

The ROS scavenging capability of  $\text{CeO}_2\text{-Fe}_3\text{O}_4\text{@LDH}$  nanocomposites was further confirmed by fluorescence images. ROS levels were directly measured by DCF-DA. As shown in Figure 4c, macrophages exhibited a green fluorescence signal indicating they were stimulated by 0.5 mM  $\text{H}_2\text{O}_2$  to produce excessive ROS. The fluorescence signal was much lower in the macrophages treated with  $\text{CeO}_2\text{-Fe}_3\text{O}_4\text{@LDH}$  nanocomposites compared to the ones without NP treatment, implying that the  $\text{CeO}_2\text{-Fe}_3\text{O}_4\text{@LDH}$  nanocomposites had ability to quench ROS.

Although  $\text{CeO}_2$  NPs were observed to perform similar to the nanocomposites when scavenging ROS, the advantages of the nanocomposite system lie in its multifunction and longer circulation time. It was reported that small nanodrugs like  $\text{CeO}_2$  NPs with sizes <6 nm can be eliminated from the blood circulation quicker than the larger NPs.<sup>18,68</sup> In addition, the combination of both imaging agent ( $\text{Fe}_3\text{O}_4$  NPs) and therapeutic agent ( $\text{CeO}_2$  NPs) in a single nanocomposite allows the tracking of the therapeutics.

**Cytotoxicity of Nanoparticles to Macrophages and CHO Cells.** Cytotoxicity of the synthesized NPs was

**Table 2.** Composition of the Combined Nanocomposite and the Concentration of Each Component

sample	concentration ( $\mu\text{g}/\text{mL}$ )	concentration ( $\mu\text{g}/\text{mL}$ )
$\text{CeO}_2$	0.5	1.0
$\text{Fe}_3\text{O}_4$	1.0 <sup>a</sup>	2.0 <sup>a</sup>
LDH	32 <sup>b</sup>	64 <sup>b</sup>
$\text{CeO}_2\text{:Fe}_3\text{O}_4\text{:LDH}$ 1:4:4	33.5 (contain 0.5 $\mu\text{g}/\text{mL}$ of $\text{CeO}_2$ )	67 (contain 1.0 $\mu\text{g}/\text{mL}$ of $\text{CeO}_2$ )

<sup>a</sup>Concentration of  $\text{Fe}_3\text{O}_4$  calculated based on the ratio between  $\text{CeO}_2$  and  $\text{Fe}_3\text{O}_4$  loading on LDH (1:2) determined by ICP-MS. <sup>b</sup>Concentration of LDH calculated based on the ratio between  $\text{CeO}_2$  and LDH (1:64) determined by ICP-MS.

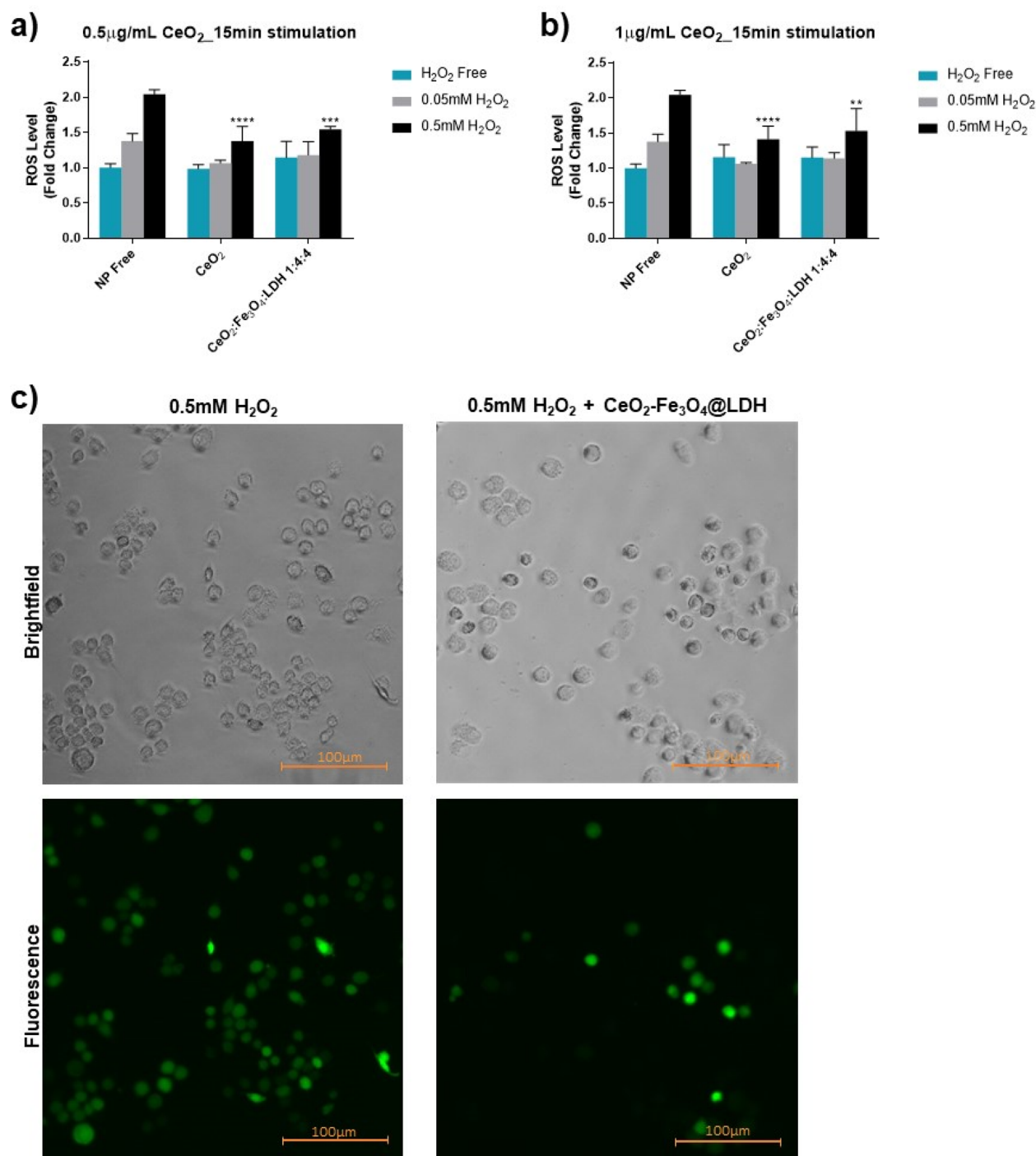


**Figure 4.** Comparison of ROS scavenging capability among different NPs. (a, b) Macrophages were pretreated with CeO<sub>2</sub>, and CeO<sub>2</sub>-Fe<sub>3</sub>O<sub>4</sub>@LDH (1:4:4) or without NP treatment, followed by stimulating by H<sub>2</sub>O<sub>2</sub> at the concentration of 0.05 mM and 0.5 mM for 15 min. (c) Bright-field and fluorescence images of macrophages were taken after NP treatment for 24 h. Macrophages were pretreated with CeO<sub>2</sub>-Fe<sub>3</sub>O<sub>4</sub>@LDHs (with CeO<sub>2</sub> concentration of 0.5 μg/mL) and without the NPs, followed by H<sub>2</sub>O<sub>2</sub> stimulating at the concentration of 0.5 mM for 15 min. Results were analyzed by two-way ANOVA. Data are presented as mean ± SD \**p* < 0.05 versus NP free control, \*\**p* < 0.01 versus NP free control, \*\*\**p* < 0.001 versus NP free control, \*\*\*\**p* < 0.0001 versus NP free control, *n* = 3.

preliminarily investigated by studying the effect of the NPs on cell viability. It was conducted with macrophage and CHO cells incubated with different concentrations of the NPs. Figure 5a showed that there was no significant cytotoxicity observed at CeO<sub>2</sub> concentrations from 0 to 0.5 μg/mL in CeO<sub>2</sub>-Fe<sub>3</sub>O<sub>4</sub>@LDH nanocomposites (concentrations ranging from 0 to 33.5 μg/mL), but a higher CeO<sub>2</sub> concentration (1 μg/mL) led to a slight decrease of macrophage viability (approximately 10%).

Compared with CHO cells at CeO<sub>2</sub> concentration of 1 μg/mL, all NPs showed no toxicity (Figure 5b). The cytotoxicity for macrophages was further confirmed by the bright-field cell imaging (Figure 5c). The morphology of macrophages was generally characteristically circular and fusiform,<sup>69</sup> as shown in the groups with CeO<sub>2</sub> concentration ranging from 0.1 to 0.5 μg/mL. However, the shape of macrophages started to change at the CeO<sub>2</sub> concentration of 1 μg/mL. These results indicate

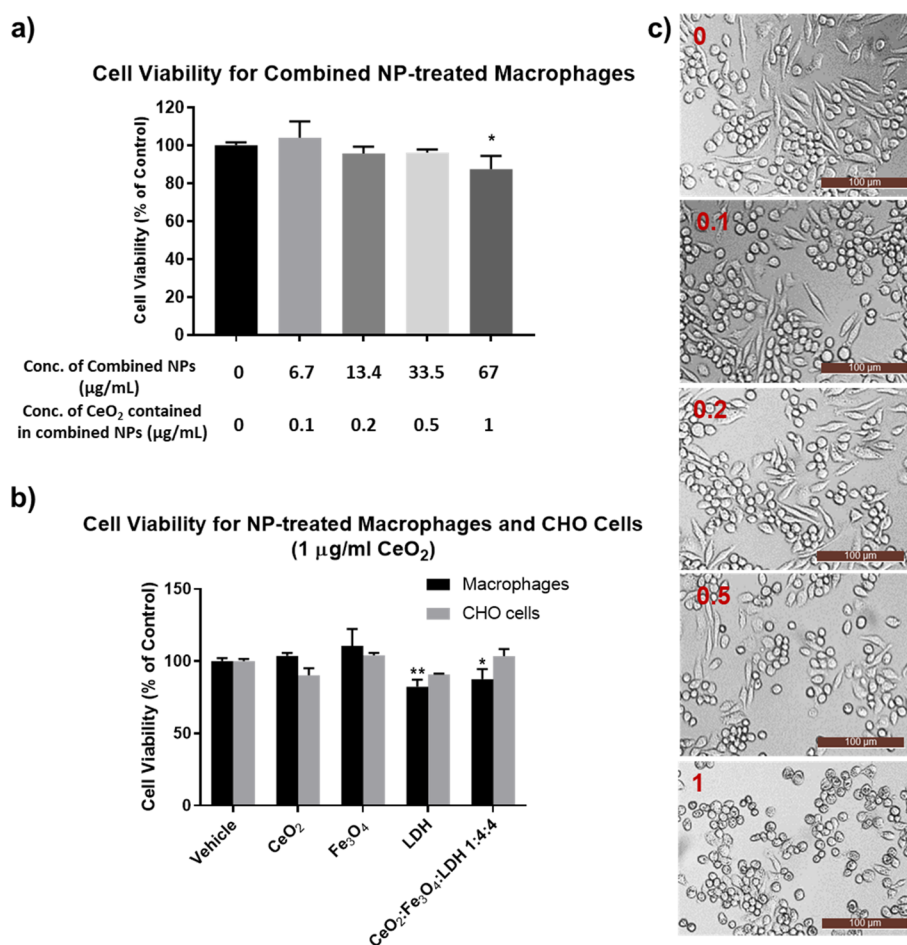


**Figure 5.** Cytotoxicity of different NPs to macrophages and CHO cells. (a) Cell viability of macrophages treated with the CeO<sub>2</sub>-Fe<sub>3</sub>O<sub>4</sub>@LDH nanocomposites with CeO<sub>2</sub> concentration ranging from 0 to 1 µg/mL (concentration of CeO<sub>2</sub>-Fe<sub>3</sub>O<sub>4</sub>@LDH nanocomposites ranging from 0 to 67 µg/mL). (b) Comparison of cytotoxicity of different NPs with the CeO<sub>2</sub> concentration of 1 µg/mL examined in macrophages and CHO cells. (c) Bright-field microscopy images for CeO<sub>2</sub>-Fe<sub>3</sub>O<sub>4</sub>@LDH nanocomposites-treated macrophages with CeO<sub>2</sub> concentration ranging from 0 to 1 µg/mL. Results were analyzed by one-way or two-way ANOVA. Data are presented as mean ± SD \**p* < 0.05 versus vehicle, \*\**p* < 0.01 versus vehicle, *n* = 3.

that CeO<sub>2</sub>-Fe<sub>3</sub>O<sub>4</sub>@LDH nanocomposites have no significant cytotoxicity on the cells at the CeO<sub>2</sub> concentration below 1 µg/mL. When the concentration of CeO<sub>2</sub> reached up to 1 µg/mL, the CeO<sub>2</sub>-Fe<sub>3</sub>O<sub>4</sub>@LDH nanocomposites showed some cytotoxicity to macrophages but not to CHO cells. It implies that these NPs could have the potential ability to induce macrophage cell death without harming normal somatic cells, which may subsequently quench the inflammatory reactions at the site. However, more study is needed to investigate this aspect.

**MRI of CeO<sub>2</sub>-Fe<sub>3</sub>O<sub>4</sub>@LDH Nanocomposites in Macrophages.** MR signals of CeO<sub>2</sub>-Fe<sub>3</sub>O<sub>4</sub>@LDH nanocomposites at different concentrations were first investigated. The conversion for concentrations between Fe and Fe<sub>3</sub>O<sub>4</sub>NPs is shown in Table 3. MRI images of the CeO<sub>2</sub>-Fe<sub>3</sub>O<sub>4</sub>@LDH nanocomposites are shown in Figure 6. CeO<sub>2</sub>-Fe<sub>3</sub>O<sub>4</sub>@LDH nanocomposites in 1% agarose gel or water exhibited the increasing *T*<sub>2</sub> contrast signals as the Fe concentration increased (Figure 6a,c). The *T*<sub>2</sub>-weighted relaxivity determined in the 1% agarose gel (144.92 mM<sup>-1</sup> s<sup>-1</sup>) was lower than that in the water (243.46 mM<sup>-1</sup> s<sup>-1</sup>) in Figure 6b,d, indicating that the surrounding environment affects the nanomaterial relaxivity.

After determining the CeO<sub>2</sub>-Fe<sub>3</sub>O<sub>4</sub>@LDH nanocomposites as the contrast agent for MRI, further *in vitro* investigation on the underlying CeO<sub>2</sub>-Fe<sub>3</sub>O<sub>4</sub>@LDH nanocomposites as the

**Table 3. Conversion for Concentrations between Fe and Fe<sub>3</sub>O<sub>4</sub>NPs Based on the Effective Concentrations of CeO<sub>2</sub> NPs Determined by ROS Quenching Activity**

concentration of CeO <sub>2</sub> (µg/mL)	concentration of Fe <sub>3</sub> O <sub>4</sub> <sup>a</sup> (µg/mL)	[Fe], mM
0.2	0.4	0.005
0.5	1	0.013
1	2	0.027
5	10	0.131
10	20	0.260

<sup>a</sup>Concentration of Fe<sub>3</sub>O<sub>4</sub> calculated based on the ratio between CeO<sub>2</sub> and Fe<sub>3</sub>O<sub>4</sub> loading on LDH (1:2) determined by ICP-MS.

contrast agent in the macrophages was conducted. The cells were incubated with the nanocomposites, then collected and evenly embedded in agarose gel for MRI. As shown in Figure 6e,f, the MRI signal of cells incubated with NPs at Fe concentrations of 0.013 mM and 0.027 mM could be readily detected corresponding to the darker color in *T*<sub>2</sub>-weighted MR images, implying the application of these nanocomposites for labeling and tracking macrophages *in vivo*.

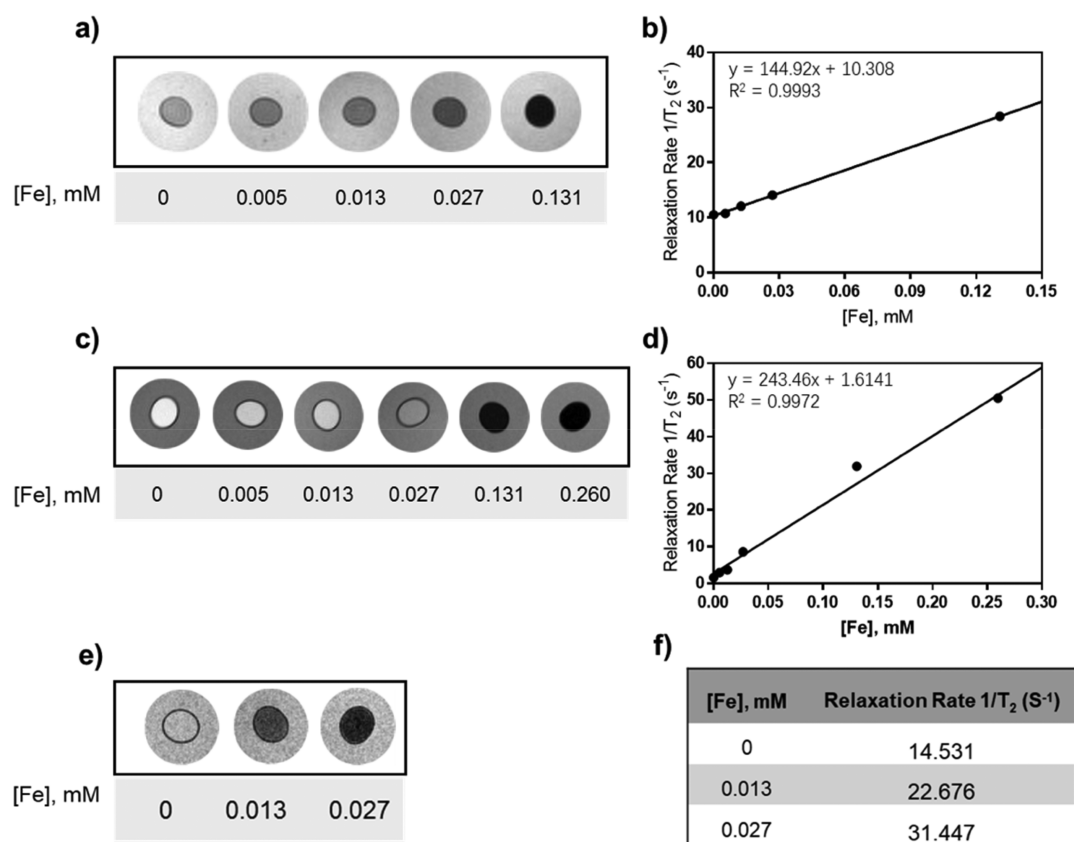


**Figure 6.** MRI of  $CeO_2-Fe_3O_4@LDHs$ . (a)  $T_2$ -weighted MR images of NP solution prepared in 1% agarose gel. (b) Plot of  $1/T_2$  over Fe concentration of  $CeO_2-Fe_3O_4@LDHs$  prepared in 1% agarose gel. (c)  $T_2$ -weighted MR images of NP solution prepared in water. (d) Plot of  $1/T_2$  over Fe concentration of  $CeO_2-Fe_3O_4@LDHs$  prepared in water. (e)  $T_2$ -weighted MR images of macrophages incubated with  $CeO_2-Fe_3O_4@LDH$  nanocomposites at different Fe concentrations. (f) Table of  $1/T_2$  over Fe concentration of  $CeO_2-Fe_3O_4@LDH$  nanocomposites in macrophages.

## CONCLUSIONS

The multifunctional  $CeO_2-Fe_3O_4@LDHs$  have been successfully developed for ROS scavenging and imaging in macrophages. The optimal mass ratio between  $CeO_2$ ,  $Fe_3O_4$ , and LDHs should be 1:4:4 due to the highest loading mass of both  $CeO_2$  and  $Fe_3O_4$  NPs on the surface of LDHs compared to other NPs synthesized at different mass ratios. In *in vitro* studies,  $CeO_2-Fe_3O_4@LDH$  nanocomposites have proven to have antioxidant properties determined by ROS scavenging activity in the macrophages. The cytotoxicity assay of this nano-hybrid shows there remains no cytotoxicity to macrophages and CHO cells at concentrations where ROS can be significantly scavenged. In MRI,  $CeO_2-Fe_3O_4@LDH$  nanocomposites exhibit good magnetic resonance signal in the macrophages, making it a potential contrast agent for cell imaging.

Current treatments for ROS-related diseases such as atherosclerosis and rheumatoid arthritis are performed systemically, leading to low therapeutic efficacy. With the development of the NP-mediated delivery system, therapeutic and diagnostic agents are allowed to be delivered locally and simultaneously. Theranostics approach or co-loading of therapeutic agents with imaging agents allows the monitoring and tracking of the drug location and distribution. In this study, the co-loading of  $Fe_3O_4$  NPs (imaging agents) and  $CeO_2$  NPs (therapeutic agents) on LDH nanocarriers enables the tracking of  $CeO_2$  NP distribution. This approach also potentially increases the circulation retention time of the small  $CeO_2$  NPs, eventually enhancing the chance that the NPs get to the target areas. Our studies have

demonstrated the applications of functionalized LDH nanocomposites *in vitro*. Further studies in animal models need to be performed to test the feasibility and efficacy of these LDH nanocomposites *in vivo*. A co-delivery strategy in combination with targeted molecules and therapeutic drugs can also be developed to enhance the therapeutic efficacy, stability, detection sensitivity, and pharmacokinetics of nanocomposites to the tissues we target. Future studies are expected to deliver NPs more specifically to the lesions where diseases form and develop. We are anticipating a broader application for the LDH nanocomposites.

## ASSOCIATED CONTENT

### Supporting Information

The Supporting Information is available free of charge at <https://pubs.acs.org/doi/10.1021/acsabm.9b00852>.

Table S1: Comparison of particle size and  $\zeta$  potential of  $CeO_2-Fe_3O_4@LDH$  nanocomposites between different mass ratios. Figure S1: XRD patterns of  $Fe_3O_4$  and  $CeO_2$ , LDH, and  $CeO_2-Fe_3O_4@LDH$  nanocomposites at a mass ratio of 1:4:4. Figure S2: Characteristics of different mass ratios of  $CeO_2@LDHs$  and  $Fe_3O_4@LDHs$ . Figure S3: EDS spectrum of  $CeO_2-Fe_3O_4@LDH$  nanocomposites at a mass ratio of 1:4:4. Figure S4: Characteristics of different mass ratios of  $CeO_2-Fe_3O_4@LDH$  NPs. Figure S5: ROS scavenging capability of  $CeO_2$  NPs (PDF)

## ■ AUTHOR INFORMATION

## Corresponding Authors

\*E-mail: h.ta@uq.edu.au; hangthuta@gmail.com.

\*E-mail: l.li2@uq.edu.au.

ORCID 

Run Zhang: 0000-0002-0943-824X

Zhi Ping Xu: 0000-0001-6070-5035

Hang T. Ta: 0000-0003-1188-0472

## Notes

The authors declare no competing financial interest.

## ■ ACKNOWLEDGMENTS

This work received financial support from the Australian National Health and Medical research council (H.T.T: APP1037310). The authors would like to acknowledge the Australian National Fabrication Facility (Queensland Node) and National Imaging Facility, Centre for Advanced Imaging for access to key items of equipment. The authors gratefully thank all of the colleagues at the Australian Institute for Bioengineering and Nanotechnology and School of Pharmacy for their comments and help.

## ■ REFERENCES

- (1) D'Autréaux, B.; Toledano, M. B. ROS as signalling molecules: mechanisms that generate specificity in ROS homeostasis. *Nat. Rev. Mol. Cell Biol.* **2007**, *8*, 813.
- (2) Babior, B. M. Phagocytes and oxidative stress. *Am. J. Med.* **2000**, *109*, 33–44.
- (3) Bonomini, F.; Tengattini, S.; Fabiano, A.; Bianchi, R.; Rezzani, R. Atherosclerosis and oxidative stress. *Histol. Histopathol.* **2008**, *23*, 381–390.
- (4) Singh, U.; Jialal, I. Oxidative stress and atherosclerosis. *Pathophysiology* **2006**, *13*, 129–142.
- (5) Hitchon, C. A.; El-Gabalawy, H. S. Oxidation in rheumatoid arthritis. *Arthritis Res. Ther* **2004**, *6*, 265–278.
- (6) Acharya, A.; Das, I.; Chandhok, D.; Saha, T. Redox regulation in cancer: a double-edged sword with therapeutic potential. *Oxid. Med. Cell. Longevity* **2010**, *3*, 23–34.
- (7) Salmon, A. B.; Richardson, A.; Pérez, V. I. Update on the oxidative stress theory of aging: does oxidative stress play a role in aging or healthy aging? *Free Radical Biol. Med.* **2010**, *48*, 642–655.
- (8) Lum, H.; Roebuck, K. A. Oxidant stress and endothelial cell dysfunction. *Am. J. Physiol Cell Physiol* **2001**, *280*, C719–741.
- (9) Newsholme, P.; Haber, E.; Hirabara, S.; Rebelato, E.; Procópio, J.; Morgan, D.; Oliveira-Emilio, H.; Carpinelli, A. R.; Curi, R. Diabetes associated cell stress and dysfunction: role of mitochondrial and non-mitochondrial ROS production and activity. *J. Physiol.* **2007**, *583*, 9–24.
- (10) Martin, K.; Barrett, J. Reactive oxygen species as double-edged swords in cellular processes: low-dose cell signaling versus high-dose toxicity. *Hum. Exp. Toxicol.* **2002**, *21*, 71–75.
- (11) Thannickal, V. J.; Fanburg, B. L. Reactive oxygen species in cell signaling. *Am. J. Physiol Lung Cell Mol. Physiol* **2000**, *279*, L1005–1028.
- (12) Apel, K.; Hirt, H. Reactive oxygen species: metabolism, oxidative stress, and signal transduction. *Annu. Rev. Plant Biol.* **2004**, *55*, 373–399.
- (13) Alfadda, A. A.; Sallam, R. M. Reactive oxygen species in health and disease. *J. Biomed. Biotechnol.* **2012**, *2012*, 936486.
- (14) Tsai, J. H.; Chen, H. W.; Chen, Y. W.; Liu, J. Y.; Lii, C. K. The protection of hepatocyte cells from the effects of oxidative stress by treatment with vitamin E in conjunction with DTT. *J. Biomed. Biotechnol.* **2010**, *2010*, 486267.
- (15) Maioli, E.; Greci, L.; Soucek, K.; Hyzdalova, M.; Pecorelli, A.; Fortino, V.; Valacchi, G. Rottlerin Inhibits ROS Formation and Prevents NFB Activation in MCF-7 and HT-29 Cells. *J. Biomed. Biotechnol.* **2009**, *2009*, 742936.
- (16) Samuhasaneeto, S.; Thong-Ngam, D.; Kulaputana, O.; Suyasanant, D.; Klaikeaw, N. Curcumin decreased oxidative stress, inhibited NF-kappaB activation, and improved liver pathology in ethanol-induced liver injury in rats. *J. Biomed. Biotechnol.* **2009**, *2009*, 981963.
- (17) Cecere, F.; Iuliano, A.; Albano, F.; Zappelli, C.; Castellano, I.; Grimaldi, P.; Masullo, M.; De Vendittis, E.; Ruocco, M. R. Diclofenac-induced apoptosis in the neuroblastoma cell line SH-SY5Y: possible involvement of the mitochondrial superoxide dismutase. *J. Biomed. Biotechnol.* **2010**, *2010*, 801726.
- (18) Xu, C.; Qu, X. Cerium oxide nanoparticle: a remarkably versatile rare earth nanomaterial for biological applications. *NPG Asia Mater.* **2014**, *6*, No. e90.
- (19) Das, M.; Patil, S.; Bhargava, N.; Kang, J. F.; Riedel, L. M.; Seal, S.; Hickman, J. J. Auto-catalytic ceria nanoparticles offer neuro-protection to adult rat spinal cord neurons. *Biomaterials* **2007**, *28*, 1918–1925.
- (20) Karagkiozaki, V.; Logothetidis, S.; Pappa, A. M. Nanomedicine for Atherosclerosis: Molecular Imaging and Treatment. *J. Biomed. Nanotechnol.* **2015**, *11*, 191–210.
- (21) Zhang, Y.; Koradia, A.; Kamato, D.; Papat, A.; Little, P. J.; Ta, H. T. Treatment of atherosclerotic plaque: perspectives on theranostics. *J. Pharm. Pharmacol.* **2019**, *71*, 1029–1043.
- (22) Yusof, N. N. M.; McCann, A.; Little, P. J.; Ta, H. T. Non-invasive imaging techniques for the differentiation of acute and chronic thrombosis. *Thromb. Res.* **2019**, *177*, 161–171.
- (23) Ta, H. T.; Arndt, N.; Wu, Y.; Lim, H. J.; Landeen, S.; Zhang, R.; Kamato, D.; Little, P. J.; Whittaker, A. K.; Xu, Z. P. Activatable magnetic resonance nanosensor as a potential imaging agent for detecting and discriminating thrombosis. *Nanoscale* **2018**, *10*, 15103–15115.
- (24) Gaston, E.; Fraser, J. F.; Xu, Z. P.; Ta, H. T. Nano- and micro-materials in the treatment of internal bleeding and uncontrolled hemorrhage. *Nanomedicine* **2018**, *14*, S07–S19.
- (25) Wu, Y.; Yang, Y.; Zhao, W.; Xu, Z. P.; Little, P. J.; Whittaker, A. K.; Zhang, R.; Ta, H. T. Novel iron oxide–cerium oxide core–shell nanoparticles as a potential theranostic material for ROS related inflammatory diseases. *J. Mater. Chem. B* **2018**, *6*, 4937–4951.
- (26) Ta, H. T.; Li, Z.; Wu, Y.; Cowin, G.; Zhang, S.; Yago, A.; Whittaker, A. K.; Xu, Z. P. Effects of magnetic field strength and particle aggregation on relaxivity of ultra-small dual contrast iron oxide nanoparticles. *Mater. Res. Express* **2017**, *4*, 116105.
- (27) Ta, H. T.; Li, Z.; Hagemeyer, C. E.; Cowin, G.; Zhang, S.; Palasubramaniam, J.; Alt, K.; Wang, X.; Peter, K.; Whittaker, A. K. Molecular imaging of activated platelets via antibody-targeted ultra-small iron oxide nanoparticles displaying unique dual MRI contrast. *Biomaterials* **2017**, *134*, 31–42.
- (28) Ta, H. T.; Prabhu, S.; Leitner, E.; Jia, F.; Putnam, K.; Bassler, N.; Peter, K.; Hagemeyer, C. Antibody-sortagging: a universal approach towards targeted molecular imaging and cell homing in cardiovascular disease. *Circ. Res.* **2011**, *107*, e37–e38.
- (29) Ta, H. T.; Li, Z.; Hagemeyer, C.; Wu, Y.; Lim, H. J.; Wang, W.; Wei, J.; Cowin, G.; Whittaker, A.; Peter, K. Novel bionanotechnological solutions based on metal oxide and metal to preserve and assess organs for transplantation. *Cryobiology* **2018**, *81*, 233.
- (30) Ta, H. T.; Li, Z.; Hagemeyer, C.; Cowin, G.; Palasubramaniam, J.; Peter, K.; Whittaker, A. Self-confirming molecular imaging of activated platelets via iron oxide nanoparticles displaying unique dual MRI contrast. *Atherosclerosis* **2017**, *263*, No. e146.
- (31) Ta, H. T.; Prabhu, S.; Leitner, E.; Jia, F.; Putnam, K.; Bassler, N.; Peter, K.; Hagemeyer, C. E. Targeted molecular imaging and cell homing in cardiovascular disease via antibody-sortagging. *Atherosclerosis* **2015**, *241*, No. e26.
- (32) Hagemeyer, C. E.; Alt, K.; Johnston, A. P.; Such, G. K.; Ta, H. T.; Leung, M. K.; Prabhu, S.; Wang, X.; Caruso, F.; Peter, K. Particle generation, functionalization and sortase A–mediated modification

with targeting of single-chain antibodies for diagnostic and therapeutic use. *Nat. Protoc.* **2015**, *10*, 90.

(33) Ta, H. T.; Peter, K.; Hagemeyer, C. E. Enzymatic antibody tagging: toward a universal biocompatible targeting tool. *Trends Cardiovasc. Med.* **2012**, *22*, 105–111.

(34) Ta, H. T.; Prabhu, S.; Leitner, E.; Jia, F.; Putnam, K.; Bassler, N.; Peter, K.; Hagemeyer, C. Antibody-sorting: a universal approach towards targeted molecular imaging and cell homing in cardiovascular disease. *Circ. Res.* **2010**, *107*, e37–e38.

(35) Ta, H.; Prabhu, S.; Leitner, E.; Putnam, K.; Jia, F.; Bassler, N.; Peter, K.; Hagemeyer, C. A novel biotechnological approach for targeted regenerative cell therapy and molecular imaging of atherothrombosis. *Heart, Lung Circ.* **2010**, *19*, S10.

(36) Ta, H. T. Activatable Magnetic Resonance Nanosensor as a Potential Imaging Agent for Detecting and Discriminating Thrombosis. *Atheroscler. Suppl.* **2018**, *32*, 159.

(37) Phinikaridou, A.; Andia, M. E.; Lacerda, S.; Lorrio, S.; Makowski, M. R.; Botnar, R. M. Molecular MRI of atherosclerosis. *Molecules* **2013**, *18*, 14042–14069.

(38) Chen, F.; Ehlerding, E. B.; Cai, W. Theranostic nanoparticles. *J. Nucl. Med.* **2014**, *55*, 1919–1922.

(39) McCarthy, J. R.; Jaffer, F. A.; Weissleder, R. A macrophage-targeted theranostic nanoparticle for biomedical applications. *Small* **2006**, *2*, 983–987.

(40) Win, K. Y.; Ye, E.; Teng, C. P.; Jiang, S.; Han, M. Y. Engineering polymeric microparticles as theranostic carriers for selective delivery and cancer therapy. *Adv. Healthcare Mater.* **2013**, *2*, 1571–1575.

(41) Lakshminarayanan, R.; Ye, E.; Young, D. J.; Li, Z.; Loh, X. J. Recent advances in the development of antimicrobial nanoparticles for combating resistant pathogens. *Adv. Healthcare Mater.* **2018**, *7*, 1701400.

(42) Ruiz-Hitzky, E.; Darder, M.; Aranda, P.; Ariga, K. Advances in biomimetic and nanostructured biohybrid materials. *Adv. Mater.* **2010**, *22*, 323–336.

(43) Li, L.; Li, B.; Gu, W.; Xu, Z. P. Modifying layered double hydroxide nanoparticles for tumor imaging and therapy. *Clays Clay Miner.* **2019**, *67*, 72–80.

(44) Li, L.; Zhang, R.; Gu, W.; Xu, Z. P. Mannose-conjugated layered double hydroxide nanocomposite for targeted siRNA delivery to enhance cancer therapy. *Nanomedicine* **2018**, *14*, 2355–2364.

(45) Li, L.; Gu, W.; Chen, J.; Chen, W.; Xu, Z. P. Co-delivery of siRNAs and anti-cancer drugs using layered double hydroxide nanoparticles. *Biomaterials* **2014**, *35*, 3331–3339.

(46) Zhang, C.; Li, L.; Han, F. Y.; Yu, X.; Tan, X.; Fu, C.; Xu, Z. P.; Whittaker, A. K. Integrating Fluorinated Polymer and Manganese-Layered Double Hydroxide Nanoparticles as pH-activated (19) F MRI Agents for Specific and Sensitive Detection of Breast Cancer. *Small* **2019**, *15*, No. 1902309.

(47) Cao, Z.; Li, B.; Sun, L.; Li, L.; Xu, Z. P.; Gu, Z. 2D Layered Double Hydroxide Nanoparticles: Recent Progress toward Preclinical/Clinical Nanomedicine. *Small Methods* **2019**, *0*, 1900343.

(48) Xu, Z. P.; Stevenson, G. S.; Lu, C. Q.; Lu, G. Q.; Bartlett, P. F.; Gray, P. P. Stable suspension of layered double hydroxide nanoparticles in aqueous solution. *J. Am. Chem. Soc.* **2006**, *128*, 36–37.

(49) Li, L.; Gu, Z.; Gu, W.; Liu, J.; Xu, Z. P. Efficient drug delivery using SiO<sub>2</sub>-layered double hydroxide nanocomposites. *J. Colloid Interface Sci.* **2016**, *470*, 47–55.

(50) Li, L.; Gu, W.; Liu, J.; Yan, S.; Xu, Z. P. Amine-functionalized SiO<sub>2</sub> nanodot-coated layered double hydroxide nanocomposites for enhanced gene delivery. *Nano Res.* **2015**, *8*, 682–694.

(51) Prasad, C.; Tang, H.; Liu, W. Magnetic Fe<sub>3</sub>O<sub>4</sub> based layered double hydroxides (LDHs) nanocomposites (Fe<sub>3</sub>O<sub>4</sub>/LDHs): recent review of progress in synthesis, properties and applications. *Journal of Nanostructure in Chemistry* **2018**, *8*, 393–412.

(52) Hoshyar, N.; Gray, S.; Han, H.; Bao, G. The effect of nanoparticle size on in vivo pharmacokinetics and cellular interaction. *Nanomedicine (London, U. K.)* **2016**, *11*, 673–692.

(53) Li, L.; Gu, W.; Chen, J.; Chen, W.; Xu, Z. P. Co-delivery of siRNAs and anti-cancer drugs using layered double hydroxide nanoparticles. *Biomaterials* **2014**, *35*, 3331–3339.

(54) Eruslanov, E.; Kusmartsev, S. In *Advanced protocols in oxidative stress II*; Springer: New York, 2010; pp 57–72

(55) Schieber, M.; Chandel, N. S. ROS function in redox signaling and oxidative stress. *Curr. Biol.* **2014**, *24*, R453–R462.

(56) Tamizhdurai, P.; Sakthinathan, S.; Chen, S.-M.; Shanthi, K.; Sivasanker, S.; Sangeetha, P. Environmentally friendly synthesis of CeO<sub>2</sub> nanoparticles for the catalytic oxidation of benzyl alcohol to benzaldehyde and selective detection of nitrite. *Sci. Rep.* **2017**, *7*, 46372.

(57) Loh, K.-S.; Lee, Y.; Musa, A.; Salmah, A.; Zamri, I. Use of Fe<sub>3</sub>O<sub>4</sub> nanoparticles for enhancement of biosensor response to the herbicide 2, 4-dichlorophenoxyacetic acid. *Sensors* **2008**, *8*, 5775–5791.

(58) Chen, J.; Shao, R.; Li, L.; Xu, Z. P.; Gu, W. Effective inhibition of colon cancer cell growth with MgAl-layered double hydroxide (LDH) loaded 5-FU and PI3K/mTOR dual inhibitor BEZ-235 through apoptotic pathways. *Int. J. Nanomed.* **2014**, *9*, 3403–3411.

(59) Li, L.; Gu, W.; Liu, J.; Yan, S.; Xu, Z. P. Amine-functionalized SiO<sub>2</sub> nanodot-coated layered double hydroxide nanocomposites for enhanced gene delivery. *Nano Res.* **2015**, *8*, 682–694.

(60) Chelliah, M.; Rayappan, J. B. B.; Krishnan, U. M. Synthesis and characterization of cerium oxide nanoparticles by hydroxide mediated approach. *J. Appl. Sci.* **2012**, *12*, 1734–1737.

(61) Zamiri, R.; Ahangar, H. A.; Kaushal, A.; Zakaria, A.; Zamiri, G.; Tobaldi, D.; Ferreira, J. Dielectrical properties of CeO<sub>2</sub> Nanoparticles at different temperatures. *PLoS One* **2015**, *10*, No. e0122989.

(62) Panwar, V.; Kumar, P.; Bansal, A.; Ray, S. S.; Jain, S. L. PEGylated magnetic nanoparticles (PEG@Fe<sub>3</sub>O<sub>4</sub>) as cost effective alternative for oxidative cyanation of tertiary amines via CH activation. *Appl. Catal., A* **2015**, *498*, 25–31.

(63) Xu, Z. P.; Stevenson, G.; Lu, C. Q.; Lu, G. Q. Dispersion and size control of layered double hydroxide nanoparticles in aqueous solutions. *J. Phys. Chem. B* **2006**, *110*, 16923–16929.

(64) Xu, Z. P.; Niebert, M.; Porazik, K.; Walker, T. L.; Cooper, H. M.; Middelberg, A. P.; Gray, P. P.; Bartlett, P. F.; Lu, G. Q. Subcellular compartment targeting of layered double hydroxide nanoparticles. *J. Controlled Release* **2008**, *130*, 86–94.

(65) Moore, K. J.; Tabas, I. Macrophages in the pathogenesis of atherosclerosis. *Cell* **2011**, *145*, 341–355.

(66) Hirst, S. M.; Karakoti, A. S.; Tyler, R. D.; Sriranganathan, N.; Seal, S.; Reilly, C. M. Anti-inflammatory properties of cerium oxide nanoparticles. *Small* **2009**, *5*, 2848–2856.

(67) Park, E.-J.; Choi, J.; Park, Y.-K.; Park, K. Oxidative stress induced by cerium oxide nanoparticles in cultured BEAS-2B cells. *Toxicology* **2008**, *245*, 90–100.

(68) Wason, M. S.; Zhao, J. Cerium oxide nanoparticles: potential applications for cancer and other diseases. *Am. J. Transl. Res.* **2013**, *5*, 126.

(69) Douglas, S.; Tuluc, F. Morphology of Monocytes and Macrophages; *Williams Hematology*, 8ed.; The McGraw-Hill Companies: New York, 2010; Chapter 67.

## Supporting Information

### **Investigating the Use of Layered Double Hydroxide Nanoparticles as Carriers of Metal Oxides for Theranostics of ROS-related Diseases**

Yajun Liu<sup>a</sup>, Yuao Wu<sup>a</sup>, Run Zhang<sup>a</sup>, Jacinta Lam<sup>b</sup>, Jack C. Ng<sup>c</sup>, Zhi Ping Xu<sup>a</sup>, Li Li<sup>a\*</sup>, Hang T. Ta<sup>a, b\*</sup>

<sup>a</sup>Australian Institute for Bioengineering and Nanotechnology, The University of Queensland, Brisbane, Australia

<sup>b</sup>School of Pharmacy, The University of Queensland, Brisbane, Australia

<sup>c</sup>Queensland Alliance for Environment Health Sciences, The University of Queensland, Brisbane, Australia

\*Correspondence to Hang T. Ta ([h.ta@uq.edu.au](mailto:h.ta@uq.edu.au)) and Li Li ([l.li2@uq.edu.au](mailto:l.li2@uq.edu.au))

**Table S1.** Comparison of particle size and zeta potential of CeO<sub>2</sub>-Fe<sub>3</sub>O<sub>4</sub>@LDH nanocomposites between different mass ratios.

Mass Ratio of CeO <sub>2</sub> :Fe <sub>3</sub> O <sub>4</sub> :LDH	CeO <sub>2</sub> :Fe <sub>3</sub> O <sub>4</sub> :LDH 1:4:4	CeO <sub>2</sub> :Fe <sub>3</sub> O <sub>4</sub> :LDH 1:4:2	CeO <sub>2</sub> :Fe <sub>3</sub> O <sub>4</sub> :LDH 1:8:4	CeO <sub>2</sub> :Fe <sub>3</sub> O <sub>4</sub> :LDH 1:8:2
Polydispersity index	0.140±0.017	0.167±0.013	0.124±0.004	0.127±0.015
Z-average (d.nm)	170.9±0.4	166.4±1.1	150.9±2.0	138.7±0.1
Zeta potential (mV)	-18.7±0.1	-23.8±0.2	-24.1±0.2	-24.0±0.5
Concentration of CeO <sub>2</sub> on LDH (µg/ml)	7.71	2.97	5.58	2.87
Concentration of Fe <sub>3</sub> O <sub>4</sub> on LDH (µg/ml)	18.73	9.01	9.36	7.15

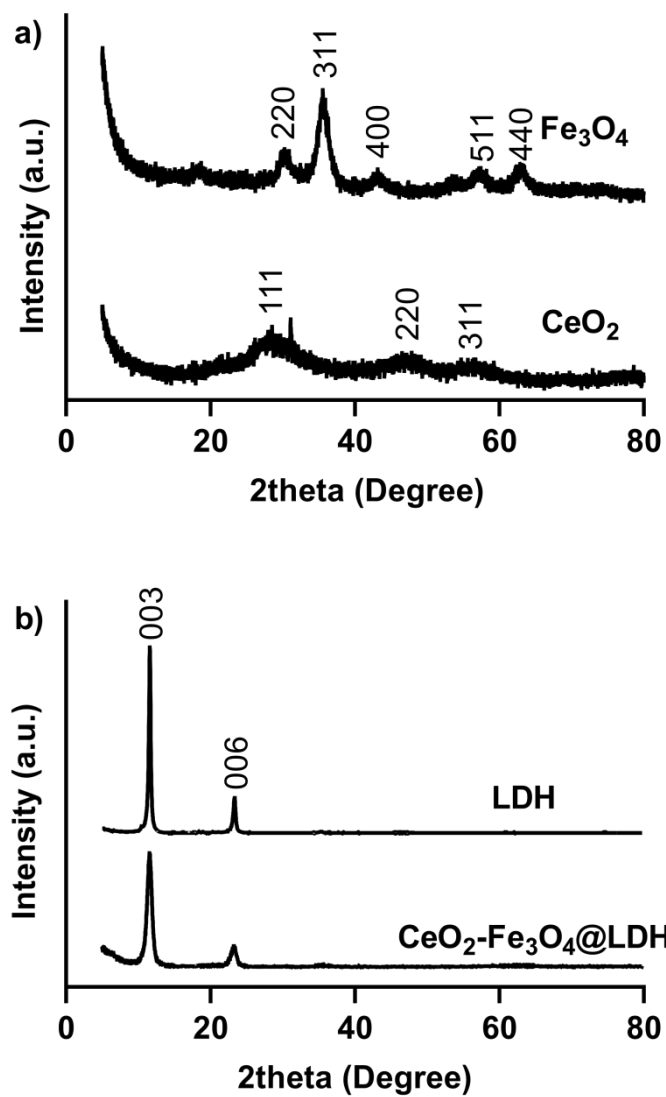


**Figure S1.** The X-ray diffraction (XRD) patterns of  $\text{Fe}_3\text{O}_4$  and  $\text{CeO}_2$  (a), LDH and  $\text{CeO}_2\text{-Fe}_3\text{O}_4\text{@LDH}$  nanocomposites at a mass ratio of 1:4:4 (b).

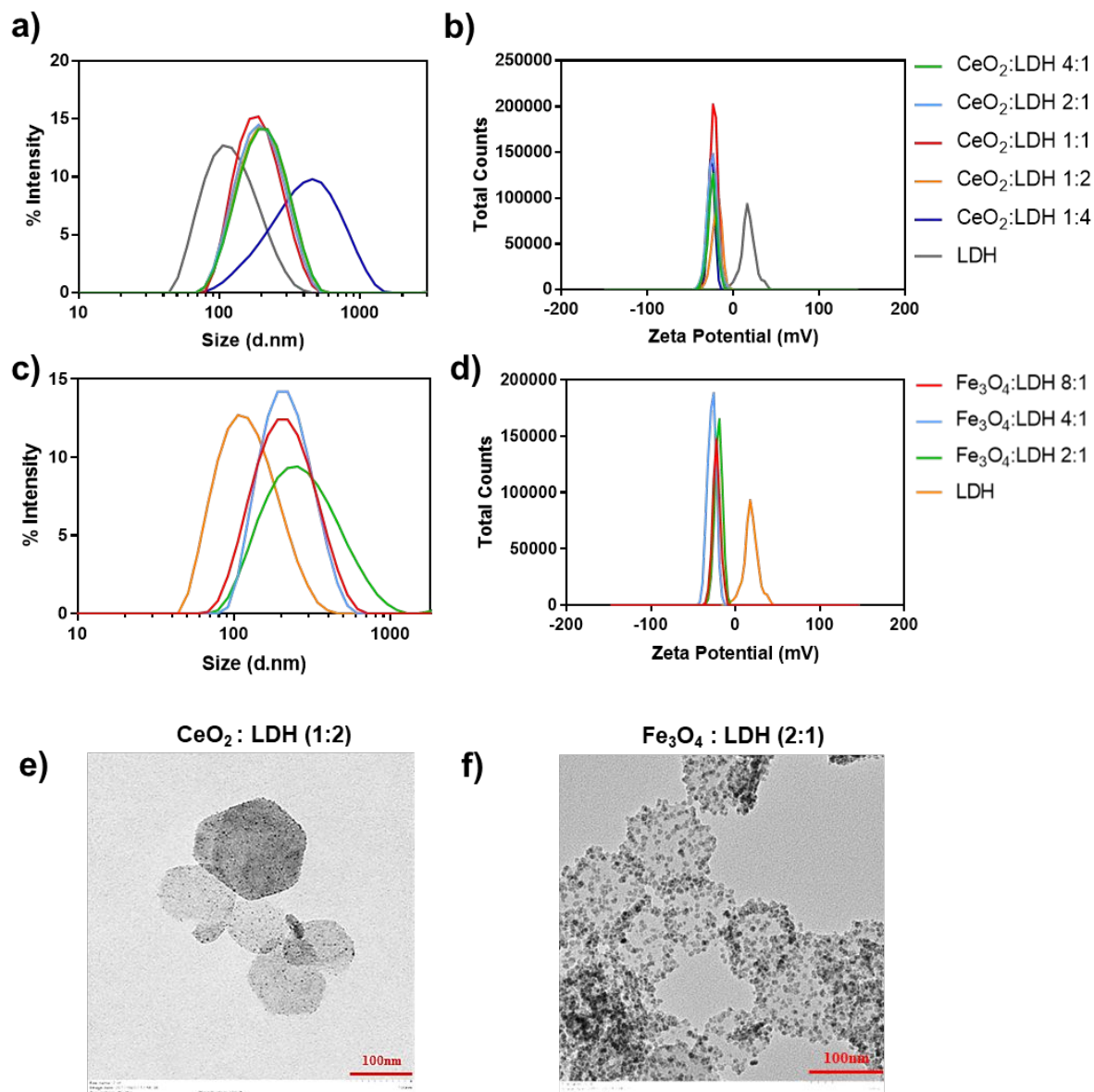


**Figure S2.** Characteristics of different mass ratios of CeO<sub>2</sub>@LDHs and Fe<sub>3</sub>O<sub>4</sub>@LDHs. (a-b) Size distribution by intensity and Zeta potential of CeO<sub>2</sub>@LDHs at different mass ratios determined by DLS. (c-d) Size distribution by intensity and Zeta potential of Fe<sub>3</sub>O<sub>4</sub>@LDHs at different mass ratios determined by DLS. (e) The TEM image of CeO<sub>2</sub>@LDHs at a mass ratio of 1:2. (f) The TEM image of Fe<sub>3</sub>O<sub>4</sub>@LDHs at mass ratio of 2:1. All the scale bars represent 100 nm.

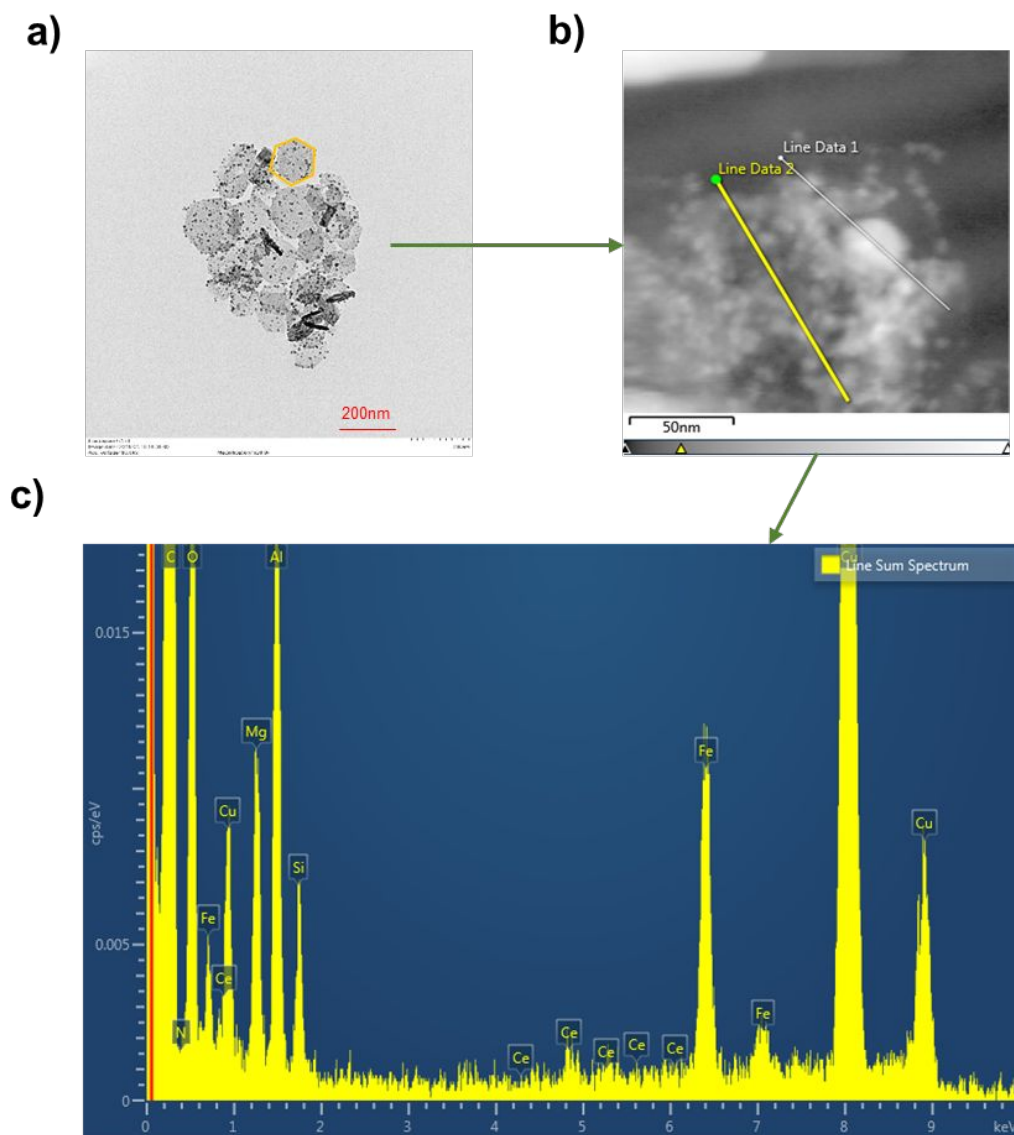


**Figure S3.** EDS spectrum of  $\text{CeO}_2\text{-Fe}_3\text{O}_4\text{@LDH}$  nanocomposites at a mass ratio of 1:4:4. (a) TEM image obtained from  $\text{CeO}_2\text{-Fe}_3\text{O}_4\text{@LDH}$  nanocomposites at a mass ratio of 1:4:4. The scale bar is 200 nm. (b) An analyzing line derived from the individual particle was drawn in yellow to be performed by EDS. (c) EDS spectrum of the individual  $\text{CeO}_2\text{-Fe}_3\text{O}_4\text{@LDH}$  nanocomposite derived from the line analyzed in (b).

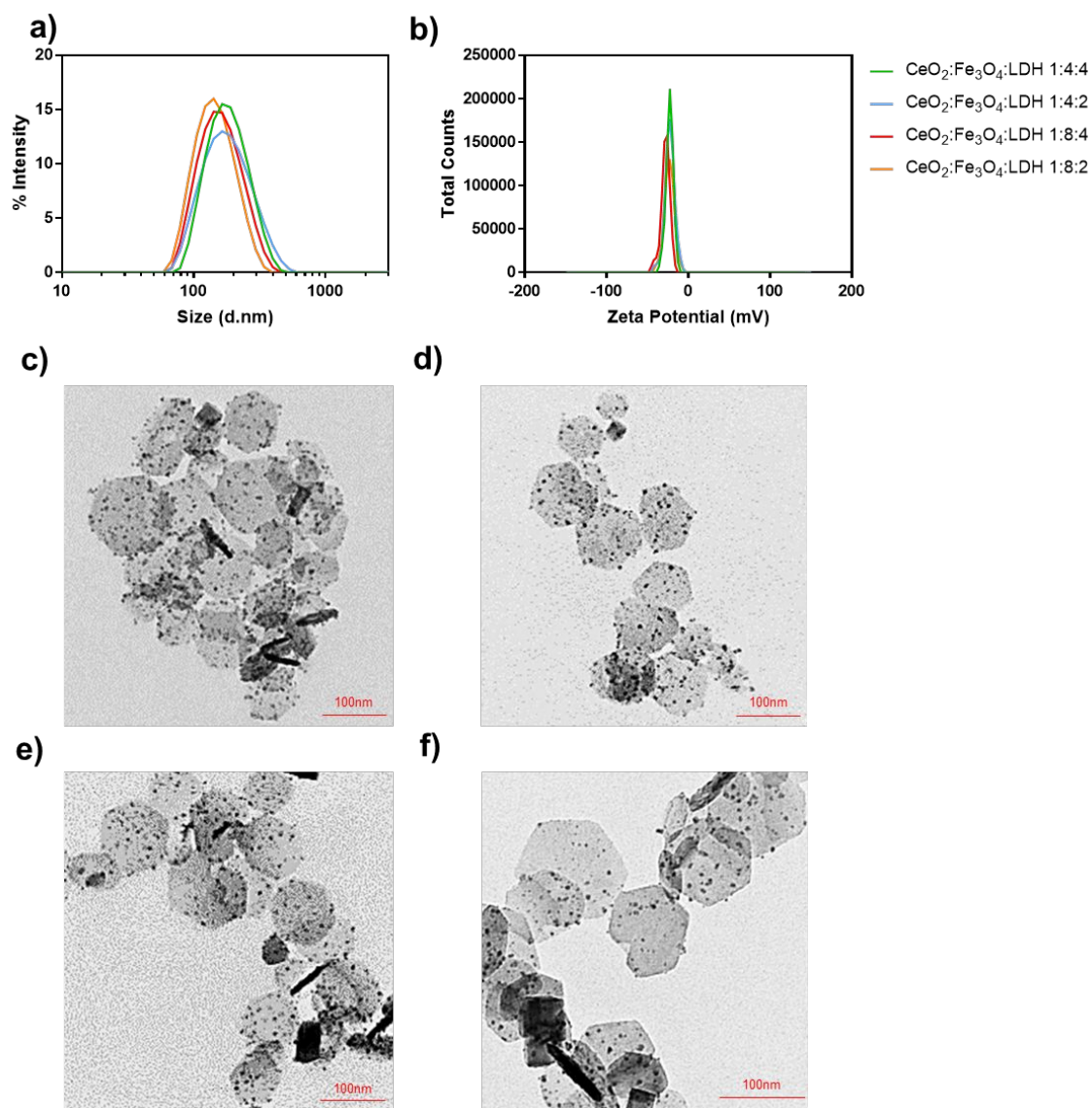


**Figure S4.** Characteristics of different mass ratios of  $\text{CeO}_2\text{-Fe}_3\text{O}_4\text{@LDH}$  nanocomposites. (a) Size distribution by intensity of  $\text{CeO}_2\text{-Fe}_3\text{O}_4\text{@LDH}$  nanocomposites at different mass ratios determined by DLS. (b) Zeta potential distribution of  $\text{CeO}_2\text{-Fe}_3\text{O}_4\text{@LDH}$  nanocomposites at different mass ratios determined by DLS. The TEM images of  $\text{CeO}_2\text{-Fe}_3\text{O}_4\text{@LDH}$  nanocomposites at a mass ratio of 1:4:4. The TEM images of  $\text{CeO}_2\text{-Fe}_3\text{O}_4\text{@LDH}$  nanocomposites at mass ratio of 1:4:4 (c), 1:4:2 (d), 1:8:4 (e) and 1:8:2 (f). All the scale bars represent 100 nm.

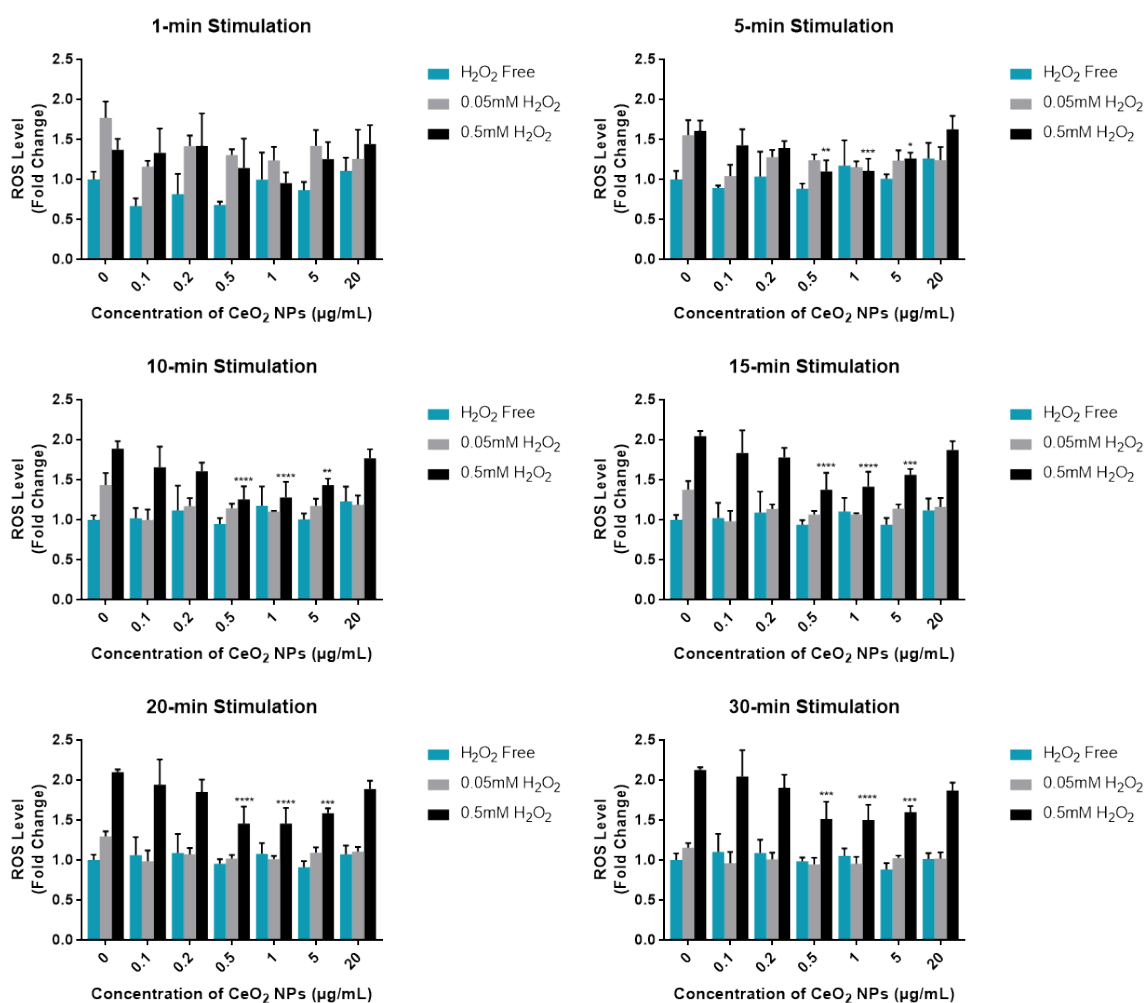


**Figure S5.** ROS scavenging capability of CeO<sub>2</sub> NPs. Graphs showing ROS levels of macrophages treated with CeO<sub>2</sub> NPs at different concentrations. Cells were stimulated with 0.05 and 0.5 mM H<sub>2</sub>O<sub>2</sub>. ROS was measured at different time points after stimulation. Results were analyzed by two-way ANOVA. Data are presented as mean  $\pm$  SD. Significant was set as \* $p < 0.05$  versus no NP control, \*\* $p < 0.01$  versus no NP control, \*\*\* $p < 0.001$  versus no NP control, \*\*\*\* $p < 0.0001$  versus no NP control,  $n = 3$ .